

001311



# Synthesis, electrical and gas sensing properties of polycrystalline ZnO films

by

Muhammad Asim Rasheed

A Thesis Submitted in Partial Fulfilment of  
the Requirements for the Degree of

Doctorate of Philosophy

Department of Physics and Physical Oceanography

Memorial University of Newfoundland

January, 2012

St. John's

Newfoundland

## Abstract

The motivation for this thesis work is to identify, assess, and address the challenges associated with the use of polycrystalline ZnO as a gas sensing material in variable humidity environments at room temperature. In this work, synthesis-structure-property relations link the chemistry and physics of the materials involved.

The effects of humidity on gas sensing are investigated by looking at three specific parameters: baseline drift, sensitivity, and response time. Ethanol, a regulated volatile organic compound, is the test gas.

In identical humidity conditions, solid state synthesized ZnO films work better as capacitive ethanol sensors than as resistive sensors, due to faster recovery times (tens of seconds), no baseline drift, and comparable sensitivities. Further capacitive sensing measurements show that increasing the humidity content of either the target gas or the sensor's environment enhances sensitivity without impacting the recovery times. In comparison, the recovery times for a test gas of water vapor alone are longer than for any ethanol-water vapor mixture. These findings suggest that water vapor may interact with the target gas, in addition to the sensing material. At very high environmental humidities (90% RH), the sensing responses for ethanol mixed with relatively dry air show surface dehydration and subsequent re-hydration in the

recovery stage due to the difference in the moisture content between the target gas and the sensor's environment.

Comparisons between the electrical properties of ZnO prepared by two different synthesis methods (solid state metathesis ZnO and Zn metal oxidation) in different humidity conditions revealed that synthesis tuning mitigates the influence of humidity on these properties. Solid state synthesized ZnO shows non-linear asymmetric current-voltage ( $I$ - $V$ ) responses at moderate (40% RH) and high (60% RH) environmental humidities, with three orders of magnitude increase in sensing current relative to dry (15% RH) conditions. In contrast, films obtained by oxidation showed less than an order of magnitude increase in sensing current under the aforementioned humidity conditions. The asymmetry in the  $I$ - $V$  responses of solid state synthesized films at moderate and high humidity is due to water electrolysis.

## Acknowledgments

*"All the praises be to ALLAH the omnipotent and magnanimous, who enabled me to complete this work and bestowed the wisdom and strength to make some contribution to the ocean of knowledge. I would also like to present thousands of Duroods and Salawa't to our Holy Prophet MUHAMMAD (Sallallahu Alaihi Wasallam), whose teachings will always guide the humankind from the darkness to light."*

I would like to express my deepest gratitude to my supervisor, Dr. Kristin M. Poduska for her guidance, patience and constant encouragement during this thesis work. She is an amazing supervisor to work with, mainly due to her ability to bring optimism and energy in the difficult times during the course of this research work. Furthermore, she encouraged me to think big, and take small but important steps in the direction of achieving the project goals. I feel in-debt to my supervisor due to her tireless effort to hone my research skills, and being so gentle in dealing with my constraints.

I would also like to thank my doctoral review committee, Dr. Martin Plumer and Dr. Qiying Chen. They have been the ones to annually monitor my progress and ensure that my research work remained on course to completion.

I would like to thank all members of Poduska research group, who are the people that I worked with and sought guidance from time to time: Shawn Chatman, Ramesh Kumar and Kitty Kumar. I would like to express my special thanks to Jiaqi Cheng,

who worked hard with me during the last year of this thesis work, and also on being the catalyst to carry this work further. I would also like to thank Dr. Erika Merschrod and her research group for their valuable input and support at various junctures during this work. Gordon Whelan (Physics workshop) deserves a special mention for his great technical support to my work as well as for our research group in general. I would not like to forget Jack Foley from Physical Oceanography workshop for his assistance in small, but important things during my stay in this department.

I would also like to thank Dr. Wanda Aylward and CREAT for XRD facilities and Dr. Liqiu Men (Biology) for SEM facilities at Memorial University of Newfoundland. I also acknowledge financial support from the Natural Science and Engineering Resource Council (Canada), Canada Foundation for Innovation New Opportunities Fund, Petroleum Research Atlantic Canada and School of Graduate Studies at Memorial University of Newfoundland.

I owe special thanks to my mother, father and all the family members for their continuous support and prayers, which helped me in completing this thesis work. In the end, I would like to thank my wife Salma, daughter Maira and son Ismail for their tireless support, patience and love that made me comfortable at my home away from home. I would express my gratitude to Marie White, a loving and caring lady from Hare Bay Newfoundland. As a neighbor, she has been a constant source of comfort to me and especially my daughter and wife. I would like to mention that people of Newfoundland look so similar in habits to my native province in Pakistan

that I would sometime forget that I am away from home.

# Contents

List of Tables	ix
List of Figures	x
<b>1 Introduction</b>	<b>1</b>
1.1 Objective and overview . . . . .	1
<b>2 Fundamentals of ZnO Synthesis, Structure and Surface Reactivity</b>	<b>8</b>
2.1 Surface chemistry and conductivity of ZnO . . . . .	8
2.2 ZnO as a gas sensing material . . . . .	10
2.2.1 ZnO band structure and gas sensing . . . . .	11
2.2.2 Review of commercial ZnO gas sensors . . . . .	17
2.3 ZnO syntheses . . . . .	20
2.3.1 Solid-state metathesis reaction . . . . .	22
2.3.2 Electrodeposition of Zn and its oxidation to ZnO . . . . .	24
<b>3 Material Characterization Techniques</b>	<b>28</b>
3.1 Diffuse Reflectance Spectroscopy . . . . .	28
3.2 X-Ray Diffraction . . . . .	32
3.3 Scanning Electron Microscopy . . . . .	35
3.4 Electrical measurements . . . . .	37
3.4.1 Current-voltage responses of ZnO . . . . .	37
3.4.2 Hysteresis effects in current-voltage responses . . . . .	42
3.4.3 Impedance spectroscopy . . . . .	44
3.4.4 Gas sensing . . . . .	47
<b>4 ZnO Preparation and Characterization</b>	<b>50</b>
4.1 Thin film production . . . . .	51
4.1.1 Metal oxidation . . . . .	51
4.1.2 Solid-state metathesis reaction . . . . .	53

4.2	Structural analysis . . . . .	54
4.3	Morphological features . . . . .	58
4.4	Optical analysis . . . . .	62
<b>5</b>	<b>Gas Sensing Responses of ZnO: The Test Case of Ethanol</b>	<b>65</b>
5.1	Resistive vs. capacitive sensing . . . . .	66
5.2	Challenges with resistive sensing . . . . .	67
5.3	Successes with capacitive sensing . . . . .	73
<b>6</b>	<b>Ambient Humidity Effects on ZnO Electrical Properties</b>	<b>76</b>
6.1	Synthesis tuning to mitigate humidity effects . . . . .	77
6.2	Impact of humidity on solid state synthesized ZnO . . . . .	80
6.2.1	DC current-voltage responses . . . . .	80
6.2.2	Impedance spectroscopy . . . . .	81
6.3	Interpreting asymmetric $I$ - $V$ responses . . . . .	83
6.3.1	Rectification . . . . .	84
6.3.2	Electrolysis . . . . .	88
6.3.3	Conclusion . . . . .	91
6.4	Implications for device applications . . . . .	91
<b>7</b>	<b>Assessing and Controlling Humidity Effects in ZnO-based Gas Sensors</b>	<b>93</b>
7.1	Quantifying ethanol detection sensitivities . . . . .	93
7.2	Reducing the impact of humidity and improving selectivity with zeolite-coatings . . . . .	102
<b>8</b>	<b>Summary, Conclusions, and Broader Contexts</b>	<b>105</b>
8.1	Summary and conclusions . . . . .	105
8.2	Future work and broader contexts . . . . .	108
	<b>Bibliography</b>	<b>112</b>
<b>A</b>		<b>129</b>
A.1	Bias dependent changes in AC impedance spectra . . . . .	129

## List of Tables

2.1	Experimental work function values of different ZnO surfaces . . . . .	9
2.2	Final enthalpies of formation for solid-state metathesis reactions based on different precursors. . . . .	24
3.1	Work function values for selected metals and different ZnO surfaces. . . . .	37
5.1	Comparison of resistive ethanol (5000 ppm) sensitivity and recovery times for ZnO films at $40 \pm 7\%$ RH. . . . .	72
5.2	Variation of capacitive ethanol sensitivity (at 5000 ppm) and recovery times at different humidities for dropcoated ZnO films. . . . .	75
6.1	Representative comparison of increase in current with relative humidity based on $I-V$ data for ZnO films prepared by solid state metathesis and Zn metal oxidation. . . . .	81
6.2	Data obtained from fitting $I-V$ responses at $40 \pm 7\%$ RH to the ideal Schottky equation. The predicted values of $\phi_B$ assume a ZnO electron affinity of 3.7 eV and $n > 1$ . . . . .	87
6.3	Data obtained from fitting $I-V$ responses of dropcoated films on steel substrate at different relative humidities to Schottky equation. . . . .	87
7.1	Variation of capacitive ethanol sensitivity (at 5000 ppm) at 40% RH for ZnO films. . . . .	99
7.2	Recovery time data for capacitive ethanol responses (at 5000 ppm) recorded at 40% RH. The water vapor (100% RH) entries correspond to water vapor injection in the chamber at 40% RH and 90% RH, respectively. . . . .	99
7.3	Variation of capacitive ethanol sensitivity (at 5000 ppm) at 90% RH for ZnO films. . . . .	101

## List of Figures

- 1.1 Representation of ZnO's wurtzite structure. Large yellow spheres correspond to oxygen and small red spheres correspond to zinc. . . . . 5
- 2.1 Band diagram of (a) bulk ZnO and (b,c) modified ZnO due to interface formation. In (b) and (c), energy is plotted along the vertical axis, and distance is along the horizontal axis. As the distance  $x$  increases, we are moving away from surface and going into the bulk of ZnO. (b) and (c) also show that band bending is restricted to  $x \leq x_0$ .  $E_C$ ,  $E_V$ ,  $E_F$ ,  $E_{F_i}$  stand for the conduction band, valence band, Fermi level and intrinsic Fermi levels.  $E_{SS}$  denote the surface states.  $q\phi_0$  denotes the energy barrier encountered by electrons to move from ZnO to the interface in (b), and vice versa in (c).  $\phi$  denotes the work function, and  $\chi$  is the ZnO electron affinity. . . . . 12
- 2.2 Potential-pH diagram showing regions of stability of  $Zn^{2+}$ , Zn, and  $Zn(OH)_2$ . The dashed line indicates the limit of water stability below which hydrogen evolution occurs. These diagrams are based on computed values of phase stabilities at 25°C temperature and 1 atmosphere pressure. It is worth noting that Zn metal is unstable in the region of potential and pH where water is stable, and hence tends to dissolve. . . . . 26
- 3.1 Schematic diagram of the light collection geometry used for diffuse reflectance spectra. . . . . 29
- 3.2 Example of (a) a UV-Vis diffuse reflectance spectrum for solid state synthesized ZnO and (b) a differentiation of the raw spectrum shown in (a). The dashed line indicates where the band gap was read from this differentiated plot. . . . . 30
- 3.3 Spread in differentiated diffuse reflectance spectra for six ZnO samples obtained by the same preparation method (Zn-metal oxidation in water). 31

3.4	Schematic diagram of Bragg's diffraction condition from two neighboring planes from the same family separated by distance $d$ . . . . .	33
3.5	Schematic diagram of the X-ray diffraction geometry. . . . .	34
3.6	Representative X-ray diffraction pattern for polycrystalline ZnO. The peaks are indexed according to the standard pattern JCPDS 36-1451. Peaks marked with an asterisk (*) are due to the stainless steel substrate. . . . .	35
3.7	Representative SEM images of polycrystalline ZnO needles at (a) low and (b) high magnification. . . . .	36
3.8	Example of an Ohmic current-voltage response. . . . .	38
3.9	Schematic depiction of an energy level diagram of a rectifying metal-semiconductor (Schottky) junction. Here $E_C$ , $E_F$ , and $E_V$ indicate the conduction band, Fermi energy, and valence band, respectively. . . . .	39
3.10	A photograph of the current-voltage measurement apparatus used in this thesis work. The set up consists of a cubical chamber (with a length of 25 cm on each side) and a sample holder with pressure contacts and external connecting leads. . . . .	41
3.11	Representative hysteretic current-voltage response for water electrolysis at a steel electrode. The arrows on this diagram indicate the direction of increasing and decreasing current with the voltage. . . . .	42
3.12	Representative (a) Nyquist plot and (b) Bode plot. . . . .	46
3.13	An example of a capacitive sensing response (along with recovery time fit) to 5000 ppm ethanol gas for a ZnO film at room temperature in a humidity controlled chamber. The rise in capacitance corresponds to the introduction of ethanol gas. . . . .	49
4.1	Schematic diagram of the three electrode electrochemical cell used for Zn electrodeposition. CE stands for counter electrode, WE stands for working electrode and RE stands for reference electrode. . . . .	52
4.2	Representative XRD patterns for (a) electrodeposited Zn and (b) ZnO obtained by oxidation of electrodeposited Zn. The peaks denoted with asterisks (*) are due to the stainless steel substrate. . . . .	55
4.3	Representative XRD patterns for ZnO powder prepared by a solid-state metathesis reaction. (a) Insufficient rinsing with water results in the leftover NaCl salt, which can be removed with rinsing with sufficient amount of ultrapure water, as shown in (b). The peaks denoted with asterisks (*) are due to the plastic sample holder in which ZnO powder was held for this measurement. . . . .	57

- 4.4 Representative SEM images of (a) electrodeposited Zn exhibiting a hexagonal plate like morphology, (b) changing to small ZnO crystallites after heating for 3 hours of oxidation (c) and into fully developed flower-like needle morphology after 6 hours of oxidation. A high magnification image of ZnO after 6 hours of oxidation reveals hollow needles (d). . . . . 59
- 4.5 Representative SEM images of ZnO particles obtained by a solid-state metathesis reaction. . . . . 61
- 4.6 Representative optical microscope luminescence images under broad spectrum illumination from a mercury lamp for (a) solid state synthesized ZnO and (b) ZnO obtained by Zn metal oxidation. The difference in the colors are likely related to different kinds of electronic defects in these materials. . . . . 63
- 5.1 (a) Representative current-voltage curve for dropcoated film at  $40 \pm 7\%$  RH showing the applied bias voltage (solid circles) at which the sensing data in (b) and (c) is taken. These films show current increases in the presence of ethanol (5000 ppm) at room temperature under (b) forward bias (at +1.5 V) or (c) reverse bias (at -1.5 V). (d) shows an example of baseline drift encountered in resistive sensing (at +400 mV). The baseline drift is evident in all cases, but the direction and magnitude of the drift are not consistent over time. The dashed vertical lines indicate when the target gas was introduced to the measurement chamber. . . . . 68
- 5.2 DC bias lowering to 400 mV (indicated by the circle in (a)), reduces the baseline drift (shown in (b)) while sensing 10000 ppm ethanol at  $40 \pm 7\%$  RH for the dropcoated film, but does not completely eliminate it. The dashed vertical lines indicate when the target gas was introduced to the measurement chamber. . . . . 70
- 5.3 Selected responses of ZnO films obtained by oxidation of Zn-metal to 5000 ppm ethanol at  $40 \pm 7\%$  RH show an incomplete recovery to baseline even at 100 mV bias voltage. The dashed vertical lines indicate when the target gas was introduced to the measurement chamber. . . . . 72
- 5.4 Selected responses of dropcoated ZnO films to 5000 ppm ethanol at (a) 15% RH (b) 40% RH (c) 65% RH. The uncertainty in RH is  $\pm 7\%$ . Dashed lines indicate when a 10 s ethanol pulse was introduced to the sensor. . . . . 74
- 6.1 Current-voltage responses for ZnO obtained by oxidation of Zn metal at relative humidities of (a)  $15 \pm 7\%$  RH, (b)  $40 \pm 7\%$  RH and (c)  $65 \pm 7\%$  RH. Each plot shows 5 sweeps. . . . . 78

6.2	SEM images of (a) ZnO obtained by a solid-state metathesis reaction, and (b) ZnO obtained by oxidation of Zn metal. Needle-like morphologies are prevalent in (b). . . . .	79
6.3	Hysteretic current <i>vs.</i> voltage responses for a drop-coated ZnO film on steel substrate at (a) 15% RH and (b) 40% RH, are likely due to the presence of adsorbed water. The arrows in (b) indicate the direction of increasing and decreasing current with the voltage. . . . .	80
6.4	Representative (a),(c) Nyquist and (b),(d) Bode plots at 15±7% RH (open circles) and 40±7% RH (solid squares) for dropcoated ZnO film. The arrows in (a) and (c) indicates the direction of increasing frequency. . . . .	82
6.5	ZnO film dropcoated on (a) Zn ( $\phi = 4.4$ eV), and (b) Co ( $\phi = 5.1$ eV) substrates tested at 40% RH show similar responses regardless of substrate work functions. . . . .	84
6.6	Example of an ideal Schottky equation fit of a current-voltage response for dropcoated ZnO at 40±7% RH. . . . .	85
6.7	Fit parameters of ZnO Schottky barrier heights ( $\phi_B$ ) and ideality factor ( $n$ ), (a) for different substrates (all at 40% RH) and (b) for changes in relative humidities (all on steel substrates). . . . .	86
6.8	Current <i>vs.</i> voltage responses for a drop-coated CuO film on a steel substrate in ambient 40% RH. . . . .	88
6.9	Example of current-voltage response (for dropcoated film of ZnO prepared by solid-state synthesis) at 40±7% RH, fit to Butler-Volmer equation. . . . .	89
6.10	Variation in fit parameters $k^0 C_O^{(1-\alpha)}$ , $C_R^0$ , and $\alpha$ (a) for dropcoated films on steel, zinc and cobalt substrates (all at 40% RH) respectively, and (b) for changes in relative humidity (all on steel substrate). The control in (a) represents the values of fit parameters for ZnO film on steel substrate in 0.1 M KCl solution without a reference electrode. . . . .	90
7.1	Variation in the responses of ZnO at 40±7% RH with different amounts of moisture mixed in 5000 ppm ethanol. A dry air pulse (with 15% RH) causes a decrease in capacitance. . . . .	95
7.2	Schematic depiction of an energy level diagram of a rectifying oxygen-semiconductor (Schottky) junction. Here $x$ denotes the distance from the surface, and $x_0$ indicates the width of the space charge region in ZnO. $E_C$ , $E_F$ , and $E_V$ indicate the conduction band, Fermi energy, and valence band, respectively. $E_{SS}$ denote the surface states, that are occupied by adsorbed oxygen species. $q\phi_b$ denotes the energy barrier encountered by electrons to move from ZnO to the surface oxygen species. $\phi$ denotes the work function, and $\chi$ is the electron affinity. . . . .	97

7.3	Representative responses of ZnO to an ethanol mixture diluted with dry air (15% RH) shows the dehydration of the films in the gradual fall below baseline and subsequent recovery to baseline. . . . .	100
A.1	Bias dependent changes in Nyquist (a,c,e) and Bode plots (b,d,f) at $40\pm 7\%$ RH from -1 V to 1 V. . . . .	130
A.2	Bias dependent changes in Nyquist (a,c,e) and Bode plots (b,d,f) at $15\pm 7\%$ RH from -1 V to 1 V. . . . .	133

# Chapter 1

## Introduction

### 1.1 Objective and overview

My approach to the materials physics is to develop a material that can do something useful. To achieve this goal, it is important to control the synthesis conditions in such a way to yield a structure with desired properties. Understanding the link between synthesis, structure and properties makes it possible to address many real-world problems. In this context, a current and applied challenge that is faced by petrochemical industries is related to methane burning. The process of petroleum production at extraction sites involves the removal of methane from crude oil reserves. Methane is dissolved in crude oil and is present in small amounts (less than 2-5 percent) in these reserves. Since this methane is not useful and costly to purify, it is separated from the crude oil and subsequently burned as it is sent through a

flare stack. If the burning of methane is complete, then only  $\text{CO}_2$  and  $\text{H}_2\text{O}$  should come out of the flarestack, as given by Equation 1.1.



However, if the separation of methane from the crude oil is not efficient then there is the possibility of other products like ethanol, carbon monoxide and hydrogen sulfide to be emitted from the flarestack during this process. Thus, there is a need to monitor products that are generated during the burning of inefficiently separated methane. This could be beneficial for the owners of the industries, as they will know if the combustion reaction is going on efficiently or not. That in turn helps them to fix the problems and save the energy spent on the incomplete combustion reaction. The other incentive to monitor these products is from environmental and health perspectives, as the governments want to control the emission of toxic species into the environment. However, the monitoring of these products is not trivial due to possible interference from steam, ambient humidity and temperature. Therefore, my thesis work is motivated by the challenge of developing a gas sensing material that can selectively detect a single gas in such a complex environment. This problem is not at all trivial and needs much effort.

In general, gas sensors are used to monitor levels of toxic gases such as carbon monoxide (at home), nitrogen oxides, carbon dioxide and volatile organic compounds

(at industrial sites) [1-3]. Due to the wide range of possible target gases, it is useful to develop materials that provide selective and repeatable gas monitoring in a variety of environments. Ideally, sensing materials should exhibit fast response and recovery times, good sensitivity and selectivity for a single test gas, environmental stability, low operating power and adaptability to different temperature ranges [4, 5]. As gas sensing is a surface reaction, the selection of material for gas sensing also depends on its characteristics surface structure and whether it is reactive to the gas that needs to be monitored. The size, shape and morphology of the material also determine its sensitivity to the target gas. Finally, depending on whether we need to monitor electrical, optical, or other property changes due to gas sensing events our choice of material may be different.

Although much fundamental research has focused on metal oxides in electrical gas sensing studies, their practical use has been somewhat limited [4, 6]. This limitation is due to a variety of factors such as low sensitivity at room temperature, lack of selectivity, drifting baseline and lack of studies in close-to-real operating environments [6]. Despite knowledge that factors such as humidity affect the properties of oxide-based sensing materials [5, 7], there is a lack of focus in addressing this situation. One possible remedy to minimize interference from unintended signals is to control surface reactivity by tuning crystallite sizes and morphologies [8]. Another strategy to improve selectivity to a particular target gas is to filter the incoming gas stream with a chemically selective coating that overlays the sensor element [9, 10].

Gas sensing materials are typically used as either resistive or capacitive sensing elements [5, 11]. Such sensors work on the principle that exposure to a target gas causes a change in either the electrical resistance or dielectric properties, respectively, of the sensing element. Metal oxides have been studied extensively as resistive gas sensors, but less so as capacitive gas sensors [4, 12, 13]. Resistive-based gas sensors can suffer from high operating resistances, which necessitates large voltages for sensor usage [14]. Capacitive gas sensors do not suffer from these problems, but the electronics required for transducing the dielectric response changes tend to be more costly to implement [4].

This thesis work investigates the effect of a wide range of ambient humidities on the electrical and gas sensing responses of polycrystalline zinc oxide (ZnO). My aim is to highlight the challenges associated with the use of ZnO as a gas sensing material in variable humidity environments, and to use correlated synthesis–structure–property studies to identify possible remedies.

ZnO is a II–VI compound semiconductor with a direct band gap in the range of 3.40 eV to 3.10 eV [15–18]. It has a hexagonal wurtzite structure, as shown in Figure 1.1, with lattice constant values of  $a = 3.250 \text{ \AA}$  and  $c = 5.207 \text{ \AA}$  [15, 19]. In this wurtzite structure, each oxygen ion ( $O^{2-}$ ) is surrounded by four zinc ions ( $Zn^{2+}$ ). The wurtzite structure of ZnO is the stable phase at all temperatures up to its melting point (1977 °C), at normal atmospheric pressure [15, 20–22]. ZnO in its native form (with no intentional doping) is an *n*-type semiconductor [23]. The

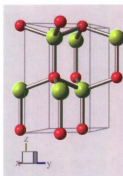


Figure 1.1: Representation of ZnO's wurtzite structure. Large yellow spheres correspond to oxygen and small red spheres correspond to zinc.

source of this *n*-type conductivity is still controversial and has often been attributed to defects (including Zn interstitials and O vacancies) or shallow donors such as hydrogen [15, 21, 24]. ZnO is a promising material in devices like light emitting diodes [15], transparent conductive films [25], solar cells [26] and gas sensors [4]. Despite decades of research, comprehensive knowledge of the surface reactivity of ZnO is still not in hand [27, 28]. Since ZnO shows slight solubility in water and relative instability in high ambient humidities [29, 30], the nature of this metal oxide-based sensor's environment can broadly affect its electrical behavior [5, 16, 28, 31].

ZnO has been synthesized by techniques such as metal-organic chemical vapor deposition [32], molecular beam epitaxy [33], thermal decomposition [34] and pulsed laser deposition [35]. These methods require high temperatures and/or high vacuum. On the other hand, solid-state metathesis reaction synthesis [12] is promising due

to its high throughput possibilities even at room temperature and pressure. Furthermore, this method offers an advantage of being translated from the laboratory scale to the industrial scale very easily. It has been used by others to tune crystallite morphologies and to produce substrate-free ZnO [12, 18, 36–41]. Another technique that allows the synthesis of both substrate-free and substrate-supported materials with a variety of sizes and morphologies is metal oxidation by gas/solid phase or liquid/solid phase reactions [42–44].

In this thesis, I describe my work on the impact of ambient humidity on the electrical and gas sensing behavior of ZnO synthesized by two different methods. Chapter 2 describes the fundamentals behind gas sensing and ZnO syntheses, and Chapter 3 describes techniques and instruments used for ZnO characterization. In Chapter 4, I discuss the structural, morphological and optical properties as well as growth of polycrystalline ZnO. Chapter 5 illustrates the problems associated with resistive sensing of ethanol in ambient temperature and humidity conditions. I demonstrate that ZnO films give repeatable and faster ethanol sensing responses when used as capacitive sensors compared to their use as resistive sensors. In Chapter 6, I show that ZnO synthesis conditions play a critical role in determining the electrical responses of ZnO in different humidities. Chapter 7 describes collaborative work with Jiaqi Cheng (PhD student in the Poduska research group) to quantify the effects of water vapor on ethanol sensing capabilities of ZnO in variable ambient and gas humidity environments. This chapter also describes strategies to eliminate the am-

bient and gas humidity effects on the sensing responses of our samples. Chapter 8 summarizes my work on the challenges with and strategies for using ZnO films as sensor materials in variable humidity environments. This chapter also gives future directions for understanding and mitigating the effects of water vapor on the surface properties of ZnO.

Synthesis studies on oxidation of Zn metal in water has evolved into a manuscript entitled "A new route to additive-free ZnO synthesis in water" that is under preparation for submission to *Crystal Growth and Design*. The capacitive ethanol sensing studies with different humidity contents in the environment as well as in the target gas have resulted in a manuscript entitled "Humidity enhances capacitive sensing by polycrystalline ZnO at room temperature", that has been submitted to *Sensors and Actuators B: Chemical* in August 2011. Furthermore, I have also contributed to a paper entitled "Electronic signatures of spatial heterogeneities in ZnO electrodeposits", which was submitted to *Applied Physics Letters* in September 2011.

## Chapter 2

# Fundamentals of ZnO Synthesis, Structure and Surface Reactivity

ZnO is an attractive semiconductor from both fundamental and applied research perspectives. To use ZnO as a gas sensing material, it is important to know the operating principles behind sensors and what material properties are desirable for their sensing elements. This chapter outlines the physics fundamentals relevant for using ZnO as a gas sensing element.

### 2.1 Surface chemistry and conductivity of ZnO

ZnO has diverse surface chemistry. In an hexagonal structure, ZnO has polar and non-polar surfaces. The polar surfaces are Zn-terminated (0001) and oxygen termi-

Table 2.1: Experimental work function values of different ZnO surfaces

ZnO surface	Work function (eV)
Zn-terminated (000 $\bar{1}$ )	3.6 [46]
O-terminated (000 $\bar{1}$ )	4.8 [46]
Mixed-terminated (10 $\bar{1}$ 0)	4.5 [46]

nated (000 $\bar{1}$ ) [27]. The non-polar surfaces are mixed terminated (with equal number of Zn cations and O anions) and include (10 $\bar{1}$ 0) and (11 $\bar{2}$ 0) [45]. The experimental work function value for each ZnO surface is also different, as shown in Table 2.1 [46]. Consequently, these ZnO surfaces interact differently with various species such as water vapor, carbon dioxide or other gases [8, 27, 47]. Studies by others with single crystals of ZnO in ultra high vacuum conditions show that the polar surface (000 $\bar{1}$ ) has strong water dissociation that results in hydroxylation of the surface [27]. The interaction of water molecules with a mixed terminated surface (10 $\bar{1}$ 0) shows only adsorption and not dissociation, based on desorption data collected at 67 °C [27]. These differences in surface reactivities have been exploited in gas sensing studies to attain improved gas selectivity [8]. For instance, it has been found that a mixed terminated (10 $\bar{1}$ 0) surface shows much higher sensitivity to ethanol [8] compared to other gases (such as ammonia and hydrogen), when tested at temperature of 300 °C.

One of the reasons that surface reactivity studies on ZnO are so complex is that it typically has a high  $n$ -type conductivity even in its native form, when no

intentional dopants are added. This is true even for single crystals of ZnO studied and prepared under controlled environments [15, 21, 24, 48]. First principles studies show that hydrogen is the cause of  $n$ -type doping [21]. This finding was later supported experimentally by Strzhemechny *et al.* based on luminescence and Hall-effect data for a single crystal of ZnO [49]. However, in another study, Look *et al.* investigated hydrothermally grown  $c$ -axis oriented ZnO and did not find the H-related donors on the surface of ZnO [48]. The controversy about the origin of  $n$ -type conductivity is not the focus of this thesis, but it dramatically increased the scientific community's interest in ZnO and its electronic properties.

## 2.2 ZnO as a gas sensing material

Many recent review articles have been dedicated to gas sensing using metal oxides. Some of these articles have provided crucial insights into this problem. For example, a review by Barsan and Weimer deals with surface adsorption processes and conduction model for polycrystalline metal oxides such as  $\text{SnO}_2$  and ZnO [50]. Another article from the same group outlines the initial steps (such as the use of the AC, DC, spectroscopic, and microscopic measurements) for understanding the detection of CO in the presence of humidity with polycrystalline metal oxide sensors [7]. Wang *et al.* provide a consolidated list of factors (such as the chemical composition, microstructure, and temperature) that influence sensitivity in such sensors [51].

Christof Wöll's paper deals with the changes in the structure and bonding of different crystallographic surfaces of ZnO due to the adsorption of gases such as hydrogen, water vapor and carbon monoxide [27]. In the following subsections, I will summarize the most relevant points (like the effects of sensing on band structure, and the factors that affect sensitivity) pertaining to ZnO gas sensors.

### 2.2.1 ZnO band structure and gas sensing

To understand the physics behind gas sensing, it is important to know how the band structure of ZnO is modified at interfaces. Figure 2.1a shows a bulk energy band diagram of ZnO [52]. Since ZnO is *n*-type in its native form, the Fermi level is located close to the conduction band. The electron concentration in the conduction band is given by Equation 2.1 [52].

$$n_d = n_i \exp\left(\frac{E_F - E_{Fi}}{kT}\right) \quad (2.1)$$

Here  $n_d$  is the density of donor atoms,  $n_i$  is the intrinsic carrier concentration,  $E_F$  is the Fermi energy,  $E_{Fi}$  is the intrinsic Fermi energy,  $k$  is the Boltzmann constant, and  $T$  is the temperature.

In general, when two materials are brought in contact with each other, equilibrium is established through the equalization of their respective Fermi levels, and the shape of the ZnO bands is altered. If the Fermi level of the interface material is lower than that of ZnO, then there is a transfer of electrons from the later to the

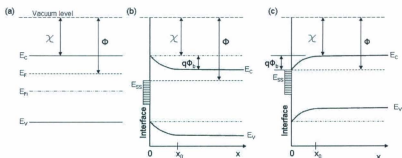


Figure 2.1: Band diagram of (a) bulk ZnO and (b,c) modified ZnO due to interface formation. In (b) and (c), energy is plotted along the vertical axis, and distance is along the horizontal axis. As the distance  $x$  increases, we are moving away from surface and going into the bulk of ZnO. (b) and (c) also show that band bending is restricted to  $x \leq x_0$ .  $E_C$ ,  $E_V$ ,  $E_F$ ,  $E_{Fi}$  stand for the conduction band, valence band, Fermi level and intrinsic Fermi levels.  $E_{SS}$  denote the surface states.  $q\phi_b$  denotes the energy barrier encountered by electrons to move from ZnO to the interface in (b), and vice versa in (c).  $\phi$  denotes the work function, and  $\chi$  is the ZnO electron affinity.

former, which causes the ZnO bands to bend (Figure 2.1b [50]). These electrons are trapped in surface states, which causes a depletion of free carriers at the interface. Likewise, if the Fermi level of the interface material is higher than that of ZnO, then electrons will transfer from the interface material to the ZnO, and bands will be altered according to Figure 2.1c [52]. This will cause an accumulation of electrons at the interface region. As a result of this equilibrium, a potential is established near the surface of ZnO, which inhibits further flow of electrons from or to ZnO. The distance over which this potential is seen within ZnO is denoted by  $x_0$  (as shown in Figure 2.1b and c). Due to the electric field present in the  $x \leq x_0$  region, there are practically no free carriers over this distance. Hence this region is called the space charge region. The potential created by the interface material in the ZnO is determined by Poisson's equation (shown here in one dimensional form), assuming that the effect of this potential extends to some point  $x_0$  in ZnO [52,53].

$$\frac{d^2V(x)}{dx^2} = \frac{-\rho(x)}{\epsilon} = -\frac{dE_{(x)}}{dx} \quad (2.2)$$

In Equation 2.2,  $V_{(x)}$  denotes the electric potential in ZnO due to the interface material,  $E_{(x)}$  is the electric field,  $\rho_{(x)}$  is the charge density, and  $\epsilon$  is the permittivity of ZnO. Solving Equation 2.2 under boundary conditions such that the effect of potential extends to point  $x_0$  gives the following expression for potential in ZnO:

$$V_{(x)} = \frac{qn_d}{\epsilon} \left( x_0x - \frac{x^2}{2} \right) \quad (2.3)$$

and  $E_{(x)}$  as:

$$E_{(x)} = \frac{qn_d}{\epsilon} (x - x_0) \quad (2.4)$$

It is clear from Equation 2.3 that the potential in ZnO changes quadratically with distance from the surface, as shown in Figure 2.1b,c [6, 51]. The maximum field exists at the ZnO surface ( $x=0$ ):

$$E_{(max)} = \frac{qn_dx_0}{\epsilon} \quad (2.5)$$

At  $x=x_0$ , Equation 2.3 becomes:

$$V_{(x=x_0)} = \phi_b = \frac{qn_dx_0^2}{2\epsilon} = \frac{E_{(max)}x_0}{2} \quad (2.6)$$

In Equation 2.6,  $\phi_b$  represents the barrier height. The width of the space charge region  $W$  can be extracted from Equation 2.6:

$$W = \sqrt{\frac{2\epsilon\phi_b}{qn_d}} \quad (2.7)$$

Considering a carrier concentration of  $10^{18} \text{ cm}^{-3}$ , a bulk dielectric constant of 8.8 and barrier height of 0.5 eV for ZnO, the width of this space charge region is about 20 nm [54], which is much smaller than the thickness of our  $\mu\text{m}$ -range ZnO films.

Due to charges stored in the space charge region that cannot move freely into the bulk ZnO, this region has a capacitance per unit area associated with it [53]:

$$C_{interface} = \frac{\epsilon}{W} \quad (2.8)$$

Substituting Equation 2.7 in Equation 2.8 gives a relationship for interface capacitance per unit area [55–57].

$$C_{interface} = \sqrt{\frac{qen_d}{2\phi_b}} \quad (2.9)$$

We have already seen that different crystallographic surfaces of ZnO have different work functions (Fermi levels) [46]. In polycrystalline ZnO, there are many grains, and the surface of these grains may be terminated by Zn or O or a mixture of Zn and O. Therefore, when an interface between two differently terminated grains is formed, it can result in the situations depicted in either Figure 2.1b or c. However, the surface terminations need not be ideal and differences in surface structure and composition will also change the band structure. Based on well accepted and studied models for polycrystalline ZnO, the gas sensing behavior is dominated by the interfaces shown in Figure 2.1b [50]. This is because flow of electrons is difficult from ZnO grains that are interfaced like those shown in Figure 2.1b, but is easier across the grains that are interfaced like the ones showed in Figure 2.1c.

If the interface shown in Figure 2.1b is exposed to ethanol (a reducing gas), the adsorbed molecules cause the ZnO to release electrons back from trapped surface states into the conduction band. This causes a reduction in amount of bending after ethanol adsorption, which decreases resistance of the sensor [58]. This is because the ethanol interaction at the interface weakens the potential and hence electric field in such ZnO grains. Adsorption of water vapor on such grain interfaces also causes a decrease in the resistance. Since water has a dipole associated with it, when it

adsorbs at the grain interface, its dipole will align and cause an accumulation of electrons in the space charge region. This will result in decreased band bending [7, 59].

In the case of capacitive sensing by polycrystalline ZnO, the measured capacitance value is the electrode area ( $A$ ) times the sum of the bulk ZnO capacitance, and the capacitance due to all the interfaces.

$$C_{measured} = A(C_{bulk} + \Sigma C_{interface}) \quad (2.10)$$

The bulk capacitance per unit area of ZnO can be calculated by considering bulk permittivity and thickness.

$$C_{bulk} = \frac{\epsilon}{thickness} \quad (2.11)$$

The approximate bulk capacitance value obtained for our ZnO films (thickness  $\sim 100 \mu\text{m}$  and area of  $0.5 \text{ cm}^2$ ) is about 30 pF.

Since ethanol adsorption causes an increase in interfacial capacitance due to an increase in electron concentration (Equation 2.9), it also shows up in the measured value of capacitance according to Equation 2.10. In fact, capacitive gas sensing detects changes in interfacial capacitance ( $C_{interface}$ ) due to adsorption of gas molecules at these exposed interfaces. Due to the very large dielectric constant of water (78.5) [11], the adsorption of water molecules at the grain interfaces will also increase the interfacial capacitance. As a result, the overall capacitance of ZnO increases with an increase in ambient humidity.

## 2.2.2 Review of commercial ZnO gas sensors

Commercially available gas sensors are typically based on two types of materials: oxide materials [4, 5] and conducting polymers [11, 60]. Metal oxide-based sensors (such as ZnO and SnO<sub>2</sub>), offer the advantages of thermal, mechanical and structural stability at extreme temperatures [2, 4, 7]. These metal oxides are sensitive to a wide variety of gases. They are non-toxic and easy to synthesize. On the other hand, polymer-based gas sensors (such as polypyrrole and polyaniline) work well at ambient temperatures and display higher sensitivities and shorter response times [60]. The design of these sensors is such that a polymer layer is deposited on a metal electrode and another metal electrode is coated on top the sensing layer. When a gas molecule comes in contact with the polymer, it will cause a physical or chemical change. In the case of volatile organic compounds, there is swelling in the polymer layer (which is proportional to the concentration of the gas molecules) that causes a change in resistance of the polymer. However, these polymers are averse to temperatures close to their glass transition temperatures (an equivalent of melting point in solids). [61]. In addition, the long polymer chains in their structure can break into smaller chains under repeated exposure to natural light with high ultraviolet radiation [5]. Therefore, they display more thermal and structural instabilities [60]. Another major disadvantage of polymer based sensors is that their humidity response is very high, therefore the signal due to a target gas can be lost [4].

Despite the potential advantages of metal oxide gas sensors, they have some

technological disadvantages. This is due in part to their lack of selectivity, which necessitates their calibration with a change in their installation environment [5,6]. Another reason is that they require high temperatures to achieve high sensitivities to the target gases, and hence their power consumption is high. This drives the cost of the metal oxide sensors higher than the polymer based sensors [3]. Another impediment for their application in oppressive environments comes from the integration of these sensing materials in the sensing devices. This is due to the stability issues of the associated circuitry in extreme temperatures, humidity, and wet environments [5].

There are many studies that demonstrate the use of polycrystalline ZnO as a gas sensing material [5]. It is sensitive to different classes of gases like volatile organic compounds, toxic industrial pollutants (such as SO<sub>2</sub>, H<sub>2</sub>S and NO<sub>x</sub>) and other gases (CO, O<sub>3</sub>, H<sub>2</sub> etc.) [4]. Seiyama *et al.* first reported that the conductivity of ZnO thin films increases in the presence of gases like ethanol and propane [62]. After this report there were numerous studies on the use of ZnO to detect all of the aforementioned gases [5]. The bulk of the gas sensing studies deal with improving the sensitivity to different target gases. This drive is due to the stringent regulations set by governments on the levels of different harmful gases [2].

ZnO pellets [13], thin films [63], nanoparticles [12] and nanorods [58,64] have been used in the gas sensing studies. The advantage of nanostructures is that the sensitivity to a target gas is better than in bulk structures due to their large surface-to-volume ratios [65]. For example, Wan *et al.* demonstrated that the film consisting

of ZnO nanorods (25 nm diameter) show 50 times higher sensitivity to ethanol than the bulk ZnO [58].

In addition to the size reduction, there are other methods to improve the sensitivity of ZnO sensors. For example, it has been reported that individual nanorods forming a Schottky contact with Pt show 1000 times higher sensitivity to carbon monoxide than the corresponding Ohmic contact device [66]. Other studies show that doping ZnO with metals (such as Pd and Nd) results in increased sensitivity [67, 68]. Cao *et al.* demonstrated that sensitivity to ethanol is enhanced by a factor of 2, by doping ZnO with 2 at% Nd. They attributed this increase to the promotion of dehydrogenation reaction of ethanol [67].

Some gas sensing studies report the drift in resistance baseline of a ZnO sensor [69–71]. The reason for the baseline drift is stated to be applied voltage bias induced change in the resistance, due to oxygen adsorption and desorption. When a bias voltage is applied, depending on the polarity of electrode, it facilitates oxygen adsorption or desorption. Oxygen adsorption increases the resistance over time, while oxygen desorption results in a decrease in the resistance with time [69]. Therefore, the magnitude and direction of the drift varies with the time. Other studies show that the prolonged exposure (of a few hours) of ZnO to oxygen at the desired operating temperature stabilizes the resistance baseline [70].

Like other metal oxides, the conductivity of a ZnO sensor also increases in the presence of water vapor or humidity in the environment [51, 72]. Studies by others

show that ZnO nanowires interact with species such as water vapor and  $\text{CO}_2$  [29,30]. In addition, water vapor can cause the surface of polycrystalline ZnO to be hydroxylated [72]. Moreover, these surface hydroxyl groups can react with atmospheric carbon dioxide to make amorphous  $\text{ZnCO}_3$  on the surface [29]. Hence, the properties of ZnO are greatly influenced by the presence of ambient water vapor. Since ZnO is reactive to water vapor as well as the target gas, therefore, water vapor also interferes with the gas sensing responses of ZnO [73]. However, there is lack of focus in addressing this situation in the context of gas sensing. Therefore, the motivation of this thesis work is to use a range of materials physics approaches to quantify the effects of water vapor on the electrical and gas sensing responses of ZnO.

A major challenge for metal oxides in general and ZnO in particular is the lack of selectivity, as these materials are sensitive to almost all the gases [4]. Strategies to improve selectivity is therefore an emerging area for gas sensing studies on metal oxides [9,10]. Discussion about how to improve selectivity will follow in Section 7.2.

## 2.3 ZnO syntheses

Synthesis of a material directly impacts the properties exhibited by it. There is always a quest for new synthesis approaches that are easy and translatable to a large scale. Synthesis methods explored for ZnO have included magnetron sputtering [74], chemical vapor deposition [32], molecular beam epitaxy [33], pulsed laser

deposition [35], sol-gel synthesis [75], electrodeposition [76] and hydrothermal synthesis [77, 78]. Within the last decade, solid-state metathesis reaction techniques have attracted attention as a high-yield way to synthesize oxides, nitrides and sulphides [79, 80]. Metathesis reactions exploit exothermic processes between fine powders of transition metal salts and main group salts to induce self-propagating, thermally-driven chemistry without the need for an external heat source. The resulting products are polycrystalline nanoscale particles with tunable sizes and morphologies. Thus, there is an opportunity to tailor the physical properties of the resulting metal oxide nanostructures to facilitate their use in technological applications such as gas sensors [12, 18, 36, 38–41, 81, 82]. Polycrystalline ZnO with a range of crystallite sizes and morphologies has also been obtained by Zn-metal oxidation by gas/solid phase; liquid/solid phase reactions [42–44].

In general, synthesis methods where the growth kinetics are slower yield the ZnO structures with preferred orientation [15]. For example, preferred growth along *c*-axis is commonly obtained from techniques like magnetron sputtering and molecular beam epitaxy [33, 83]. However, it must be noted that the substrates used in these techniques are also highly oriented, which could induce textured ZnO growth. Zn-metal oxidation by liquid/solid phase reactions tend to give *c*-axis oriented structures [44]. Moreover, thermal oxidation by solid/vapor method has been used to obtain ZnO nanorods and nanobelts by controlling the deposition temperature and catalyst [65]. Nanorods of ZnO have been obtained by using a catalyst; however

without it, nanobelts have been obtained [84,85]. Hydrothermal synthesis is another technique that is reported for control over sizes and morphologies of polycrystalline ZnO films. Joo *et al.* [78] were able to suppress growth along the  $c$ -axis by using ions such as Cd, Cu, Mg and Ca to form an inhibition layer on the (002) face. On other hand, nanorods with large aspect ratios were obtained by using Al, In and Ga that inhibited lateral growth.

### 2.3.1 Solid-state metathesis reaction

Polycrystalline ZnO films obtained from different synthesis techniques display a range of morphologies that depend on synthesis conditions. ZnO has three fast growing directions, which are  $\pm[0001]$ ,  $[01\bar{1}0]$  and  $[2\bar{1}\bar{1}0]$  [65]. The morphology of ZnO is dependent on relative surface activities of various growth facets under the synthesis conditions [86].

Solid-state metathesis has been successfully used to synthesize ZnO nanoparticles and nanorods at room temperature [12,37,39–41]. Such a reaction is exothermic in nature, meaning that the difference in the enthalpies of formation ( $\Delta H_f$ ) between products and reactants is negative. Considering the reactants  $\text{ZnCl}_2$  and  $\text{NaOH}$  mixed in molar ratios of 1:2, the chemical reaction is [12,87]:



$$(\Delta H_f = -47.1 \text{ kcal/mole})$$



$$(\Delta H_f = +13.2 \text{ kcal/mole})$$

This solid-state synthesis of ZnO is not limited to the aforementioned zinc salt precursor. It is possible to obtain the ZnO by reacting other zinc-based compounds with NaOH or KOH [18,36]. One possibility is  $\text{ZnSO}_4$ :



while another is  $\text{Zn(NO}_3)_2$ :



Table 2.2 summarizes the enthalpies of formation for all three reactions. In this thesis work, ZnO is obtained by the reaction between  $\text{ZnCl}_2$  and NaOH.

The morphology of solid-state synthesized ZnO can be influenced by the presence of a third reactant like sodium dodecyl sulfate (SDS), polyethyleneglycol (PEG),

Table 2.2: Final enthalpies of formation for solid-state metathesis reactions based on different precursors.

Starting salt	Final $\Delta H_f$ (kcal/mole)
ZnCl <sub>2</sub>	-33.9 [87]
ZnSO <sub>4</sub>	-34.2 [87]
Zn(NO <sub>3</sub> ) <sub>2</sub>	-44.0 [87]

cetyltrimethylammonium chloride (CTAB), or triethanolamine (TEA) [12,18,38–41]. Other studies have utilized the presence of a salt like KCl to change the particle size [36]. The addition of a third reactant can slow down the growth of ZnO in certain directions, thereby allowing the preferential growth into rod-like morphologies instead of nanoparticles [12,18,38–41]. Additional reactants can introduce new by-products, many of which can be removed by rinsing with ultrapure water, alcohol, sonication, centrifugation or oven drying [12,18,36,38–41]. The solid-state metathesis reaction technique has been used to tune electronic and optical characteristics of ZnO by changing of particle sizes and shapes [12,18,36–41].

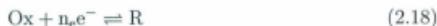
### 2.3.2 Electrodeposition of Zn and its oxidation to ZnO

Recently, ZnO has been synthesized by heating Zn metal in ultrapure water [43,44]. Zn metal can be bought from commercial sources or synthesized by different techniques. In this thesis work, an electrodeposition technique was employed to synthesize Zn metal films on steel electrodes, which were subsequently oxidized by

heating in ultrapure water.

Electrodeposition involves coating a material on the target electrode that is immersed in a suitable electrolyte (containing cations of that material) under application of potential [88]. One has to consider the pH and potential values at which chemical species are stable in that aqueous solution. This can be summarized in Pourbaix diagrams [89]. These potential *vs.* pH plots are based on thermodynamic calculations of the stability of the metal oxides, metal hydroxides, and metal ions in water. Figure 2.2 shows a simplified version of the Pourbaix diagram for  $\text{Zn}^{2+}$ , Zn, and  $\text{Zn}(\text{OH})_2$  at 25°C and 1 atmosphere [89]. The standard potentials for electrochemical reactions are shown on the  $y$ -axis and measured relative to the potential difference between a working electrode, at which the reaction occurs, and a reference electrode. In this thesis work, the electrochemical potential for electrodeposition is reported against a  $\text{Ag}/\text{AgCl}_{\text{sat'd}}$  reference.

The phase boundaries in a Pourbaix diagram indicate reduction/oxidation (redox) reactions that can occur during an electrochemical experiment.



Here 'Ox' is the oxidized species, 'R' is the reduced species, and  $n_e$  is the number of electrons transferred per reaction [90]. When the potentials are more negative than the standard reaction potential, the reduction of the 'Ox' species is more favored,

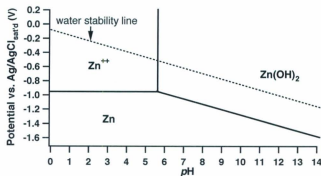


Figure 2.2: Potential-pH diagram showing regions of stability of  $\text{Zn}^{2+}$ , Zn, and  $\text{Zn}(\text{OH})_2$ . The dashed line indicates the limit of water stability below which hydrogen evolution occurs. These diagrams are based on computed values of phase stabilities at 25°C temperature and 1 atmosphere pressure. It is worth noting that Zn metal is unstable in the region of potential and pH where water is stable, and hence tends to dissolve.

while at more positive potentials the oxidation of 'R' is favored. For Zn metal electrodeposition, the standard potential is - 0.96 V *vs.* Ag/AgCl<sub>sat'd</sub>. The reduction-oxidation reaction for Zn electrodeposition can be written as [88]:



When the potentials are more negative than -0.96 V *vs.* Ag/AgCl<sub>sat'd</sub>, the formation of Zn metal is more favorable, and above this potential Zn<sup>2+</sup> ion formation (that is dissolution of Zn metal) will occur. For electrodeposition in thesis work, potential value of -1.2 V *vs.* Ag/AgCl<sub>sat'd</sub> was always selected to ensure Zn metal electrodeposition.

When Zn metal is immersed in water at ambient temperature and pressure, it has a tendency to dissolve [91]. Due to this dissolution and subsequent reaction with water, the formation of products like Zn(OH)<sub>2</sub> is possible [89]. If the temperature of water is higher than the stability temperature of Zn(OH)<sub>2</sub> ( $\geq 50^{\circ}\text{C}$ ) then it will convert to ZnO [92]. Oxidation of Zn metal to form ZnO films will be discussed in Chapter 4.

## Chapter 3

# Material Characterization Techniques

Chemical composition and surface structure play an important role in the gas sensing response of a material. We use spectroscopy, microscopy and diffraction techniques to identify the composition and bulk structure of our ZnO samples before using them in gas sensing studies. Electrical measurements, both AC and DC, also give us information about the behavior of our samples in different environments.

### 3.1 Diffuse Reflectance Spectroscopy

Diffuse reflectance spectroscopy (DRS) on our ZnO samples is done for phase confirmation. This is possible because ZnO shows a characteristic electronic band

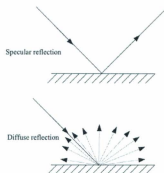


Figure 3.1: Schematic diagram of the light collection geometry used for diffuse reflectance spectra.

gap optical absorption in the range of 3.40 eV to 3.10 eV [15–18]. DRS works on the principle that, if photons with energy lower than that of the band gap are incident on a sample, no electrons can be excited into the conduction band, resulting in their reflection or transmission. If the incident photon energies are greater than those of the band gap, they are absorbed, resulting in a reduced intensity in the reflected light. The reflection is diffuse instead of specular due to the rough nature of the sample surface, as shown in Figure 3.1.

Our DRS experiments are conducted with an Analytical Instrument Systems Model DT1000 CE UV-Visible light source (200–800 nm) and an Ocean Optics SD2000 collection and analysis system. Photons are incident on the sample at an angle of  $45^\circ$  with respect to the surface normal. Before collecting spectra, the instru-

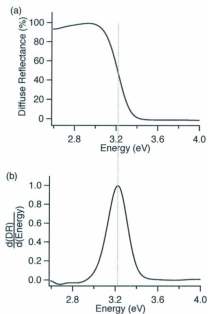


Figure 3.2: Example of (a) a UV-Vis diffuse reflectance spectrum for solid state synthesized ZnO and (b) a differentiation of the raw spectrum shown in (a). The dashed line indicates where the band gap was read from this differentiated plot.

ment is calibrated against a reference sample whose composition and surface roughness gives maximum reflectance in the aforementioned wavelength range. Thus, 100% reflectance for the sample (at a particular wavelength) means it is as reflective as this reference. The transition between absorption and reflection is often not very clear in real materials due to defects in crystal structure and different sizes of crystallites [93]. Spectra can be differentiated [93] and then the value of the maximum

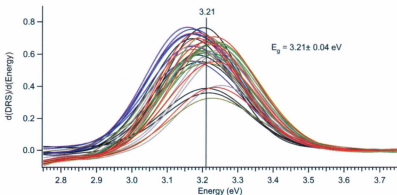


Figure 3.3: Spread in differentiated diffuse reflectance spectra for six ZnO samples obtained by the same preparation method (Zn-metal oxidation in water).

(indicating the absorption edge) is quoted, as shown in Figure 3.2. Differentiation of diffuse reflectance spectra has been reported to give more accurate and reliable measures of band gap energies [93, 94]. To obtain representative band gap values for each sample, I collect least six different spectra at different points on a single sample. The uncertainties we report for a set of samples are based on the spread among such spectra. In all cases, this spread is larger than uncertainty in reading a peak in one spectrum.

Figure 3.3 shows an example of how the band gap values were calculated for a group of six ZnO samples prepared under identical reaction conditions. The line drawn in the middle in Figure 3.3 indicates the average of these 36 different measurements.

## 3.2 X-Ray Diffraction

To learn about the crystal structure and lattice constants of our samples, X-ray diffraction was used. A crystal is a periodic array of atoms in three dimensions, which can be described as a set of basis atoms placed within a Bravais lattice. X-rays can be diffracted from electrons in a crystal. For diffraction to occur, the wavelength of the diffracted radiation must be comparable to the spacing of the lattice planes. As the lattice spacing for crystalline solids is typically on the order of Angstroms, the energy of incident X-ray photon should thus be on the order of keV. Diffraction peaks would only be observed when Bragg's diffraction condition is satisfied [95,96], as given by Equation 3.1.

$$2d \sin \theta = m\lambda \quad (3.1)$$

For diffraction to occur, the path length difference of the diffracted wave should be an integer multiple of the incident wavelength. In Equation 3.1,  $d$  is the distance between two neighboring planes,  $\theta$  is the angle of incidence of the X-rays,  $\lambda$  is the wavelength of incident X-rays and  $m$  is the order of diffraction. Figure 3.4 schematically depicts Bragg's diffraction condition [95].

A polycrystalline material has crystallites with many different orientations, so a diffraction pattern from such a material (including our ZnO) will have a range of peaks with different positions and intensities, each of which is consistent with the unit cell for that material.

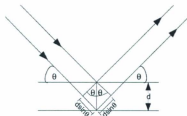


Figure 3.4: Schematic diagram of Bragg's diffraction condition from two neighboring planes from the same family separated by distance  $d$ .

XRD data for this thesis were collected with a Rigaku Ultima IV X-ray diffractometer. The typical parameters used in collecting X-ray diffraction data were a scan range of  $20\text{--}90^\circ$  in  $2\theta$  with a scan speed of  $6^\circ/\text{min}$  and step size of  $0.02^\circ 2\theta$ . The X-ray diffractometer has two primary components: a  $\text{Cu K}_\alpha$  source and a scintillation detector. A schematic diagram illustrating the working geometry of an X-ray diffractometer is shown in Fig. 3.5. The  $\text{Cu K}_\alpha$  source used to collect spectra for this thesis is operated at a voltage of 40 kV and current of 44 mA. The emitted X-ray photons from the source have a wavelength of  $1.5406 \text{ \AA}$  and are monochromatic. When these X-ray photons are incident on a crystalline material at allowed Bragg angles, the photons will be diffracted and are received by the detector. The diffracted X-ray photons excite the electrons of the detector's scintillating material, which return to their ground states by releasing photons. This information is recorded in the form

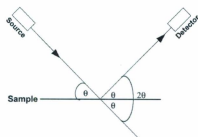


Figure 3.5: Schematic diagram of the X-ray diffraction geometry.

of intensity *versus* the angle between the sample and X-ray source.

By analyzing X-ray diffraction peak positions, the crystalline phase of samples can be confirmed. In order to do so, lattice constant refinements for ZnO samples were done by using Jade software (Materials Data Incorporated) with at least 6 peaks for each XRD pattern. Figure 3.6 shows a representative XRD pattern for polycrystalline ZnO. There are no significant crystalline impurity phases present since all peaks, except for those due to the substrate, can be indexed to the standard wurtzite ZnO pattern (JCPDS 36-1451). The Joint Committee for Powder Diffraction Studies (JCPDS), database is a reference for powder X-ray diffraction data for many crystalline materials that have been experimentally determined [19].

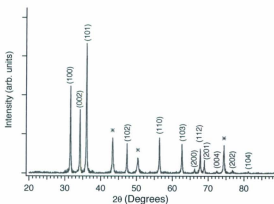


Figure 3.6: Representative X-ray diffraction pattern for polycrystalline ZnO. The peaks are indexed according to the standard pattern JCPDS 36-1451. Peaks marked with an asterisk (\*) are due to the stainless steel substrate.

### 3.3 Scanning Electron Microscopy

Scanning electron microscopy (SEM) is used to produce high resolution images of the surface morphology of our materials based on topographical changes on the surface [97]. The primary probe in SEM is an electron beam that is produced by thermionic or field emission. The electron beam is accelerated toward the sample surface in an evacuated column that contains optics such as electromagnetic condenser lenses, objective lenses for focusing the beam and electromagnetic deflection coils for moving the beam across the sample surface. When a beam of electrons is incident on the sample surface, various types of interactions occur resulting in a variety of signals [97]. These signals cannot be detected by a single detector. The most

commonly used detector collects secondary electrons. Differences in the position and depth at which the secondary electrons are emitted lead to contrast in the recorded image [98]. Samples analyzed in a SEM have to be mounted on a conducting stage to dissipate the charge that can build up during the continuous bombardment of the electron beam on the sample surface. Therefore, if a sample is poorly conductive then a conductive coating on the sample surface becomes important. The conductive coating is usually thin and of such a material that it does not interfere too much with the sample surface under analysis.

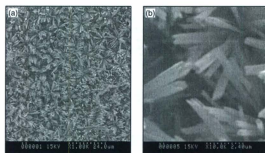


Figure 3.7: Representative SEM images of polycrystalline ZnO needles at (a) low and (b) high magnification.

Scanning electron micrographs, utilizing secondary electron imaging (Hitachi S-570), were collected on dried ZnO powders that were mounted on conductive aluminum stubs and then gold-coated. No conductive coating was required for imaging ZnO grown on metallic substrates. Figure 3.7 is an example of SEM images that

show both wide field and zoom image of the needle-like habit that is observed for ZnO films grown on a metallic substrate.

## 3.4 Electrical measurements

### 3.4.1 Current-voltage responses of ZnO

Repeatable and reliable electrical responses of ZnO are necessary to realize its use as a gas sensor. Current-voltage responses for ZnO depend on the type of metal contacts used and also the crystallographic face of ZnO on which contacts are made.

Table 3.1 show work function values of selected metals and ZnO surfaces.

Table 3.1: Work function values for selected metals and different ZnO surfaces.

Metal	Work function (eV)	ZnO surface	Work function (eV)
Aluminum	4.1 [52]	Zn-terminated (0001)	3.6 [46]
Cobalt	5.1 [99]	O-terminated (000 $\bar{1}$ )	4.8 [46]
Zinc	4.4 [100]	Mixed-terminated (10 $\bar{1}$ 0)	4.5 [46]
Gold	5.1 [100]		
Platinum	5.7 [100]		

If the work function of the metal contact is less than or equal to that of ZnO surface, then the junction should be Ohmic [52]. However, if the work function of metal contact is larger than that of ZnO surface, then the junction should be rectifying [52]. It is worth mentioning that this type of classification appears easy to predict, but surface and interfacial states often defy expectations, even when dealing

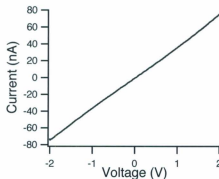


Figure 3.8: Example of an Ohmic current-voltage response.

with single crystals of ZnO. For polycrystals, a large number of different crystallographic surfaces are present, which makes it difficult to predict the junction behavior with a particular metal. For an Ohmic junction, the current linearly increases with voltage, as shown in Figure 3.8 and given by Equation 3.2.

$$V = IR \quad (3.2)$$

Low resistance Ohmic contacts to *n*-type ZnO are necessary for many electrical and optical device applications [15]. There are some literature reports that show formation of Ohmic contacts with *n*-type ZnO [101–103]. These Ohmic contacts are based on pure metals such as aluminum [103] or alloys such as Ti/Al [101], Ta/Au [102] and Al/Pt [103].

In the case of rectifying junctions, current varies non-linearly with applied voltage, and there is higher current for one polarization of the applied voltage than the other. A rectifying Schottky junction can occur at the interface between an *n*-type

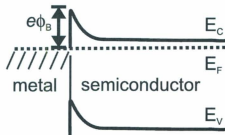


Figure 3.9: Schematic depiction of an energy level diagram of a rectifying metal–semiconductor (Schottky) junction. Here  $E_C$ ,  $E_F$ , and  $E_V$  indicate the conduction band, Fermi energy, and valence band, respectively.

semiconductor and a metal due to the difference between the Fermi energy levels in these two isolated materials. When an  $n$ -type semiconductor comes into contact with a metal, the negative charge carriers near the junction move into the metal to occupy available lower energy states. The Fermi level then becomes continuous across the two materials. The excess positive charge in the semiconductor causes a depletion (space charge) region [52]. Consequently, electrons in the metal cannot move into semiconductor freely and thus face a potential barrier (Schottky barrier,  $\phi_B$ ), which is equal to the difference between the metal work function ( $\phi_m$ ) and the electron affinity ( $\chi$ ) of the semiconductor (as given by Equation 3.3).

$$\phi_B = \phi_m - \chi \quad (3.3)$$

When a forward bias voltage is applied to the semiconductor, the barrier height

will be reduced and current will flow from the semiconductor into the metal. This current will increase as an exponential function with the increase in applied voltage, according to the idealized Schottky relation [53].

$$I = aA^*T^2 \exp\left(\frac{-e\phi_B}{kT}\right) \left[ \exp\left(\frac{e(V-IR)}{nkT}\right) - 1 \right] \quad (3.4)$$

$$I = I_s \left[ \exp\left(\frac{e(V-IR)}{nkT}\right) - 1 \right] \quad (3.5)$$

Here,  $I_s$  is the pre-exponential factor that gives the saturation current,  $a$  is the area of contact,  $A^*$  is Richardson's constant ( $32 \text{ A/cm}^2\text{K}^2$ ),  $T$  is the temperature,  $e$  is the electron charge,  $\phi_B$  is Schottky barrier height,  $k$  is Boltzmann's constant,  $V$  is the voltage,  $I$  is the current,  $R$  is the series resistance and  $n$  is the ideality factor [53, 104, 105]. When the forward current ( $I$ ) is much larger than the reverse saturation current ( $I_s$ ) then Equation 3.5 can be written as [105]:

$$I = I_s \exp\left(\frac{e(V-IR)}{nkT}\right) \quad (3.6)$$

Rectifying Schottky contacts are beneficial for some device applications such as light emitting diodes [15]. Many literature reports show that high work function metals can be used to obtain Schottky contacts, although the reported barrier heights are often lower than predicted [15]. Metals used for achieving Schottky contacts are typically gold [106], platinum [104] and palladium [107]. Schottky contacts have been subject to different surface treatments such as ozone cleaning [15] and laser irradiation [104] to improve rectification.



Figure 3.10: A photograph of the current-voltage measurement apparatus used in this thesis work. The set up consists of a cubical chamber (with a length of 25 cm on each side) and a sample holder with pressure contacts and external connecting leads.

For this thesis work, current-voltage ( $I$ - $V$ ) data were collected by sweeping the voltage from -2 V to +2 V and recording the current using either a Princeton Applied Research (PAR) EG&G Potentiostat or Hokuto Denko HA 501 potentiostat. The data were obtained and recorded using LabVIEW (National Instruments) user interfaces designed by others and modified in our group [108]. The  $I$ - $V$  measurements were done by holding samples between stainless steel pressure contacts (0.3–1.2 cm<sup>2</sup> surface area) while enclosed in a humidity-controlled chamber (Figure 3.10). Relative humidity (RH) values were measured using a digital humidity meter (La Crosse Technology) with an uncertainty of  $\pm 7\%$  RH.

### 3.4.2 Hysteresis effects in current–voltage responses

Figure 3.11 shows an example of hysteresis while measuring current–voltage response of steel electrode in an aqueous electrolyte. In  $I$ - $V$  measurements without an electrolyte, hysteresis has been attributed to electrolysis of ambient moisture on ZnO [31, 109]. Water electrolysis at positive (anode) and negative (cathode) electrodes will give rise to oxidation and reduction reactions respectively [31, 109, 110]:

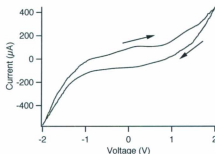


Figure 3.11: Representative hysteretic current–voltage response for water electrolysis at a steel electrode. The arrows on this diagram indicate the direction of increasing and decreasing current with the voltage.

The kinetics of the electrochemical reactions that occur at electrode surfaces are affected by the potential applied. The Butler–Volmer expression gives electrode

current and kinetic dependencies as a function of potential [88,111].

$$I = I_0 \left\{ \exp\left(\frac{-n\alpha F\Delta V}{RT}\right) - \exp\left(\frac{n(1-\alpha)F\Delta V}{RT}\right) \right\} \quad (3.9)$$

$$I_0 = nFAk^0 C_O^{(1-\alpha)} C_R^\alpha \quad (3.10)$$

In Equation 3.9,  $I_0$  is the exchange current measured in amperes,  $n$  denotes the number of electrons involved in the reaction.  $\alpha$  is the electrode kinetics parameter (transfer coefficient, defined as the fraction of free energy given by electrical energy ( $nFE$ ) that affects the reaction rate).  $F$  is the Faraday constant,  $R$  is the gas constant,  $T$  is the temperature and  $\Delta V$  is the over-voltage.  $A$  is the area of the electrode,  $k^0$  is the heterogeneous rate constant which gives the rate of charge transfer in a reaction, and  $C_O^{(1-\alpha)}$  and  $C_R^\alpha$  give oxidation and reducing species concentrations in bulk solution [88,90,112]. At large over-voltages, Equation 3.9 reduces to [111]:

$$I = I_0 \exp\left(\frac{2(1-\alpha)F\Delta V}{RT}\right) \quad (3.11)$$

or:

$$I = I_0 \exp\left(\frac{2\alpha F\Delta V}{RT}\right) \quad (3.12)$$

These Butler-Volmer expressions will be used in Chapter 6 to interpret the current-voltage responses of solid state synthesized ZnO in variable humidity environments.

### 3.4.3 Impedance spectroscopy

Impedance spectroscopy is helpful in separating bulk responses (grain interior) from surface responses (grain boundaries and contacts) in polycrystalline materials [113,114]. Impedance spectroscopy also provides useful information about the changes in electrical response of the material caused by factors such as ambient moisture. This information may be in the form of changes in conduction as a result of changes in the dielectric constant of a material [11]. In impedance spectroscopy, an AC voltage signal at a particular frequency (and at a particular DC voltage bias) is applied to the sample, and the resulting steady state current is measured [115].

$$v(t) = V_m \sin(\omega t) = V_m \exp(j\omega t) \quad (3.13)$$

$$i(t) = I_m \sin(\omega t + \theta) = I_m \exp(j\omega t - \theta) \quad (3.14)$$

In Equation 3.13,  $v(t)$  is the instantaneous voltage,  $V_m$  is the maximum amplitude,  $\omega$  is the angular frequency, and  $t$  is time. In Equation 3.14  $i(t)$  is the instantaneous current,  $I_m$  is the maximum amplitude of current and  $\theta$  represents the phase difference between current and voltage in radians. For completely resistive behavior,  $\theta$  would be zero [115]. The impedance of the system can be calculated by dividing Equation 3.13 by Equation 3.14:

$$Z(\omega) = \frac{V_m \exp(j\omega t)}{I_m \exp(j\omega t - \theta)} = Z \exp(j\theta) = Z(\cos \theta + j \sin \theta) = Z' + jZ'' \quad (3.15)$$

$Z(\omega)$  is a vector quantity composed of real and imaginary parts. The absolute magnitude of the impedance is:

$$|Z| = \sqrt{Z'^2 + Z''^2} \quad (3.16)$$

In impedance spectroscopy measurements, the data are usually displayed with the negative values of the imaginary part of the impedance plotted along the  $y$ -axis and the real part of the impedance values plotted along the  $x$ -axis. An example of this kind of (Nyquist) plot is shown in Figure 3.12a, and each point gives the values of the the real and the imaginary components of the impedance at one frequency. Data collected at higher frequencies appear on the left side of the plot and those collected at lower frequencies are displayed on the right side. The Nyquist plot has the advantage of providing the resistance contribution to the overall impedance, but a disadvantage is that frequency does not appear explicitly [115]. Another representation of the same data, is a plot of the log of absolute impedance values *versus* the log of frequency (Figure 3.12b), which is called the Bode plot [116]. The advantage of this Bode plot is that it is easy to see the dependence of impedance on the applied frequency [115]. Both Nyquist and Bode plots will be used in Chapter 6.

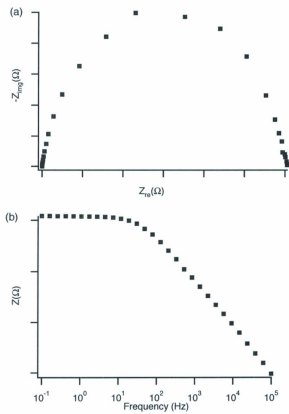


Figure 3.12: Representative (a) Nyquist plot and (b) Bode plot.

The single semicircle seen in Figure 3.12a is attributed to the grain-boundary controlled conduction and is often modeled as an equivalent circuit containing a resistor and capacitor in series [113, 117]. The resistance in such a circuit is related to the grain boundary resistance encountered by electrons, whereas capacitance is linked to the existence of depletion regions at grain boundaries [113, 118, 119].

A Princeton Applied Research (PAR) Potentiostat/Galvanostat (Model 273A with Signal Recovery Model 5210 Lock-in Amplifier) was used to apply the desired AC potential with different DC bias voltages ranging from -1 V to 1 V (1 Hz to 0.1 MHz, with an RMS amplitude of 10–25 mV). The data collection was controlled using PowerSUITE software (Princeton Applied Research). For taking impedance measurements, sample contacts were made in the same way as for  $I$ - $V$  measurements (as described in Section 3.4.1).

### 3.4.4 Gas sensing

Sensing responses to ethanol gas were measured for ZnO adhered to metallic substrates. Resistive sensing data were collected using either a Hokuto Denko HA 501 potentiostat or National Instruments LCR meter (model NI PXI-1033 with NI-4072 and modified Labview interface). Capacitive sensing data were collected by measuring charge/discharge behavior while applying an AC voltage of 50 mV at 3 kHz frequency using the aforementioned National Instruments LCR meter. The gas sensing apparatus is similar to the one described for  $I$ - $V$  measurements.

Gas sensing measurements were done in a humidity controlled chamber at room temperature ( $20 \pm 2$  °C) and the target gas pulse was introduced near the sample through a syringe. Humidity values were measured using a digital humidity meter (La Crosse Technology), and uncertainties are  $\pm 7\%$ .

For resistive sensing, sensitivities were assessed by taking a ratio of the current values, at a particular applied voltage, with and without the presence of target gas. In the case of capacitive sensing, sensitivities were computed by taking the ratio of the difference in capacitance in the presence and absence of target gas to the capacitance in ambient air. The characteristic recovery time constants after exposure to ethanol were measured by fitting with an exponential function. Figure 3.13 shows an example fit to obtain the recovery time constant for 5000 ppm ethanol sensing by a ZnO film.

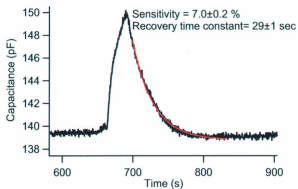


Figure 3.13: An example of a capacitive sensing response (along with recovery time fit) to 5000 ppm ethanol gas for a ZnO film at room temperature in a humidity controlled chamber. The rise in capacitance corresponds to the introduction of ethanol gas.

## Chapter 4

# ZnO Preparation and Characterization

The growth conditions during synthesis of a material has a direct impact on its crystallinity, structure and morphology. Furthermore, the structure and morphology of a material affect its properties. Polycrystalline materials have a large number of grain boundaries, and this is not ideal from an electrical properties perspective because they cause high resistances. However, polycrystals can be desirable for gas sensing applications due to their large surface area available for interactions with gas molecules [120]. With this aim, we synthesized polycrystalline ZnO by two different methods: solid state metathesis and oxidation of electrodeposited Zn-metal in ultrapure water. X-ray diffraction data show that ZnO obtained by both methods is polycrystalline and has an hexagonal wurtzite crystal structure. Scanning electron

images show that ZnO obtained by oxidation displays a needle-like morphology while solid state synthesized ZnO displays a particle-like morphology. We conclude that these differences could help explain why these two preparations yield very different ethanol sensing responses.

## 4.1 Thin film production

This thesis work involves ZnO prepared by two different methods. The first is a substrate-supported ZnO that is formed directly on a metal surface. The second is a nanocrystalline ZnO powder that can be prepared as a slurry and then coated on a metal substrate.

### 4.1.1 Metal oxidation

The electrodeposition of Zn was performed in a Pyrex glass cell with a Teflon top. The steel surface on which Zn was electrodeposited was the working electrode (WE) with a surface area  $\sim 2.3 \text{ cm}^2$ . The thickness of steel working electrode was 0.05 cm. A Hokuto Denko HA501 potentiostat was used to apply a potential to the WE with respect to a  $\text{Ag}/\text{AgCl}_{\text{sat'd}}$  reference electrode (RE). A gold wire was used as a counter electrode (CE) with a surface area  $\sim 2.5 \text{ cm}^2$ . A schematic diagram of the setup is shown in Figure 4.1 [112]. The electrolyte was 0.2 M  $\text{ZnSO}_4 \cdot 7\text{H}_2\text{O}$  (ACS reagent grade, supplied by ACP) with 0.1 M  $\text{H}_3\text{BO}_3$  (ACS reagent grade,

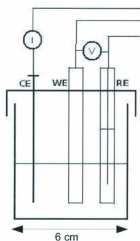


Figure 4.1: Schematic diagram of the three electrode electrochemical cell used for Zn electrodeposition. CE stands for counter electrode, WE stands for working electrode and RE stands for reference electrode.

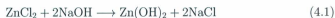
Merck) prepared in ultrapure water. The electrodeposition was carried out at room temperature ( $20 \pm 2$  °C) at a potential of  $-1.2$  V vs.  $\text{Ag}/\text{AgCl}_{\text{sat'd}}$  for 5–30 minutes.

Electrodeposited Zn films on steel substrates were oxidized in ultrapure water according to a procedure we adopted from the literature [44]. The resulting Zn-coated electrode was placed in a glass beaker with ultrapure water and heated on a hot plate to a temperature of  $95 \pm 5$  °C. I checked the DC resistance of the samples after every hour with a digital multimeter. Zn-metal oxidation was stopped when the sample resistance reached  $5\text{--}10$   $\Omega$  (after 3 hours), and when resistance exceeded

20  $\Omega$  (after 6 hours).

#### 4.1.2 Solid-state metathesis reaction

Polycrystalline ZnO powder was prepared by using a solid state metathesis reaction technique [12, 37], which has proven to be a versatile synthesis method for producing metal oxide particles with sizes  $\sim 10$ -1000 nm [18, 36, 38-41, 80]. The reaction technique described here is adapted from a procedure given in the literature [12]. ZnCl<sub>2</sub> (ACS reagent grade, Merck) and NaOH (ACS reagent grade, Caledon) were weighed separately in a 1:2 molar ratio. The salts were ground separately in agate mortars for 10-15 minutes to produce even, fine powders that were then blended together. During blending, a reaction between these salts occurs:



$$(\Delta H_f = -47.1 \text{ kcal/mole})$$



$$(\Delta H_f = +13.2 \text{ kcal/mole})$$

Taking into account the total heats of formation for the two reactions given in Equation 4.1 and Equation 4.2, the formation of ZnO is thermodynamically favorable due to the fact that the net enthalpy of formation ( $\Delta H_f$ ) is negative. The water

that comes out due to the reaction described in Equation 4.2 is in vapor form [12], although some of this vapor subsequently condenses onto ZnO as it cools. After complete reaction (1–2 minutes of stirring), the product was rinsed with large amounts of ultrapure water (18.2 M $\Omega$ -cm, Barnstead Nanopure) to remove unreacted salts and NaCl produced during the reaction. The remaining white solid was air-dried and then oven-dried at 115 °C for at least 24 hours. The resulting dried ZnO product was suspended in ethanol (95% ethanol and 5% water) to yield a concentration of 100 g/L, after which 200 ppm of HCl was added and the suspension was sonicated for 20 minutes. ZnO dropcoated films were produced by drying  $\sim$  0.3 ml on a conducting substrate (stainless steel or other substrates like Co and Zn) and then air-dried. Film thicknesses were estimated to be 100 $\pm$ 50  $\mu$ m based on calculation of the area of ZnO film and its concentration in the drop.

## 4.2 Structural analysis

The structural analysis of electrodeposited Zn and the subsequent product obtained after its oxidation in ultrapure water was done using X-ray diffraction (XRD). The transformation of electrodeposited Zn to ZnO is shown in Figure 4.2. The refined lattice constants for electrodeposited Zn ( $a = 2.663 \pm 0.001$  Å and  $c = 4.946 \pm 0.001$  Å) match well with standard values ( $a = 2.665$  Å and  $c = 4.947$  Å, JCPDS 04-0831) [19]. Refined lattice constants for ZnO ( $a = 3.252 \pm 0.002$  Å and  $c = 5.207 \pm 0.002$  Å) also

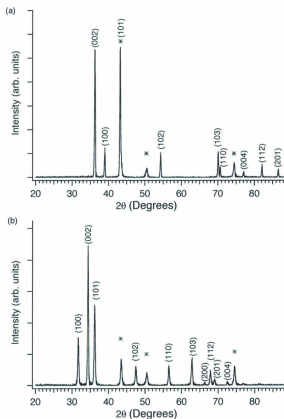


Figure 4.2: Representative XRD patterns for (a) electrodeposited Zn and (b) ZnO obtained by oxidation of electrodeposited Zn. The peaks denoted with asterisks (\*) are due to the stainless steel substrate.

match well with accepted values ( $a = 3.250 \text{ \AA}$  and  $c = 5.207 \text{ \AA}$ , JCPDS 36-1451) [19].

Solid state metathesis reactions also yield polycrystalline ZnO powder in the wurtzite structure (Figure 4.3). It is worth noting that insufficient rinsing after the solid-state reaction can lead to left-over salt in the final product (as seen in Figure 4.3a), in line with findings by other researchers [12]. Furthermore, refined lattice constants  $a = 3.252 \pm 0.001 \text{ \AA}$ ,  $c = 5.210 \pm 0.001 \text{ \AA}$  match well with accepted values ( $a = 3.250 \text{ \AA}$  and  $c = 5.207 \text{ \AA}$ , JCPDS 36-1451) [19]. We note that dispersing ZnO powder in solvents like ethanol and coating it on a substrate did not alter the ZnO X-ray diffraction patterns.

Based on X-ray diffraction data shown above, the ZnO obtained by oxidation of Zn metal gives preferred orientation compared to solid state synthesized ZnO. In solid-state synthesis, others have shown that ZnO growth can be tempered by the use of additives to obtain nanorods instead of nanoparticles [12, 38–40], but we do not explore this here.

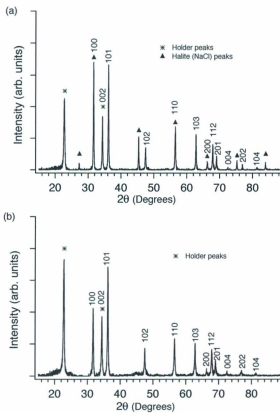


Figure 4.3: Representative XRD patterns for ZnO powder prepared by a solid-state metathesis reaction. (a) Insufficient rinsing with water results in the leftover NaCl salt, which can be removed with rinsing with sufficient amount of ultrapure water, as shown in (b). The peaks denoted with asterisks (\*) are due to the plastic sample holder in which ZnO powder was held for this measurement.

### 4.3 Morphological features

Scanning electron images reveal interesting morphological differences between electrodeposited Zn before and after oxidation. Figure 4.4a shows that electrodeposited Zn displays plate and block morphologies with a predominant hexagonal habit. These morphologies and apparent crystallite sizes are dramatically different from those obtained after the conversion to ZnO (Figure 4.4b,c,d). ZnO adopts a more acicular morphology, with many needles nucleating from a common area to yield flower-like bunching. Close inspection of the needles reveals that some are hollow tubes. In all cases, the sizes of the ZnO crystallites are much smaller than the Zn crystallites from which they started [121].

The grain size decrease during the first stage of oxidation, along with the dramatic change in crystal habit from Zn to ZnO, points to crystal growth *via* a Zn dissolution mechanism. When Zn metal is placed in water, it can dissolve, as indicated in the Pourbaix diagram given in Chapter 2 (Figure 2.2). This dissolution of Zn metal is possible even at room temperature and has been observed experimentally [43, 91]. According to Reference [91], grain edges are the most likely points where dissolution of Zn metal can occur:



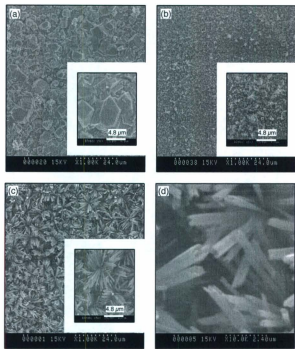


Figure 4.4: Representative SEM images of (a) electrodeposited Zn exhibiting an hexagonal plate like morphology, (b) changing to small ZnO crystallites after heating for 3 hours of oxidation (c) and into fully developed flower-like needle morphology after 6 hours of oxidation. A high magnification image of ZnO after 6 hours of oxidation reveals hollow needles (d).



Zn ions react very quickly with water molecules to form  $\text{Zn(OH)}_2$  and hydrogen is simultaneously evolved (Equation 4.4). Since the temperature in our experiment is  $95 \pm 5^\circ\text{C}$ , which is higher than the stability temperature of  $\text{Zn(OH)}_2$ , it transforms to ZnO according to Equation 4.5.

We propose that formation of ZnO could occur progressively at many grain edges, and that these ZnO crystallites grow with time [121]. Smaller crystallites and underdeveloped flower-like needles are visible after oxidation for 3 hours, as shown in Figure 4.4b. By increasing the oxidation time to 6 hours, more developed flower-like bunches are observed all over the ZnO surface (Figure 4.4c). These flower-like bunches consist of needles, as seen in Figure 4.4d. Needle-like ZnO is often observed with aqueous growth techniques [122–124].

For ZnO prepared by solid state metathesis (shown in Figure 4.5), we get much smaller particles with ill-defined faces. This is consistent with earlier reports [12]. As discussed in Section 2.3.1, different morphologies of ZnO by similar reactions have also been obtained.

The observed differences in the morphologies of the ZnO obtained by these two synthesis methods could influence their electronic behavior. This will be discussed in more detail in Chapter 6.



Figure 4.5: Representative SEM images of ZnO particles obtained by a solid-state metathesis reaction.

## 4.4 Optical analysis

Using the procedure described in Chapter 3, band gap values for our samples were calculated from diffuse reflectance measurements. For solid state synthesized ZnO, DRS data yielded band gap values of  $3.22 \pm 0.03$  eV, which overlap with values for oxidation of Zn metal ( $3.21 \pm 0.04$  eV). These values also show good agreement with reported ZnO band gap values of 3.40–3.10 eV [15–18, 21].

Although the band gap values are similar for metathesis and oxidized ZnO, interesting luminescence differences were observed when these samples were viewed under broad spectrum illumination from a mercury lamp using a Leica DM-2500 optical microscope. We note that the color rendering in the optical images printed in this thesis are a good approximation (but not perfect) to the colors seen by eye while using microscope. Solid state synthesized ZnO exhibits uniform yellow luminescence, as shown in Figure 4.6a. Yellow luminescence in ZnO is often attributed to the presence of oxygen vacancies [125, 126] or negative oxygen interstitials [127]. In contrast, three dominant types of luminescence (green, blue and orange) were observed for ZnO samples obtained by oxidation, as seen in Figure 4.6b. The green luminescence has been correlated with Zn vacancies [23]. Blue luminescence has been attributed to Zn interstitials [128], and orange luminescence has been related to oxygen interstitials [129] or fewer oxygen vacancies [125].

The assignment of various luminescence colors to different type of defects and

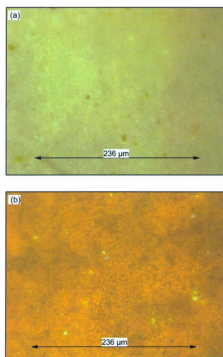


Figure 4.6: Representative optical microscope luminescence images under broad spectrum illumination from a mercury lamp for (a) solid state synthesized ZnO and (b) ZnO obtained by Zn metal oxidation. The difference in the colors are likely related to different kinds of electronic defects in these materials.

impurities is controversial, because there is not one-to-one correspondence between color and defect type [15]. In order to establish whether or not the luminescence changes seen here are related to the differences in stoichiometry, X-ray photoelectron spectroscopy of these films can be done. Therefore, substantial work is needed to determine the exact origin of the luminescence differences between ZnO prepared by these two different methods.

## Chapter 5

# Gas Sensing Responses of ZnO: The Test Case of Ethanol

The development of gas sensing materials that can repeatably and reliably sense a target gas is an ongoing challenge, especially in environments that involve variable moisture levels. With this aim, we studied gas sensing responses of polycrystalline ZnO films to ethanol (a regulated volatile organic compound [1]), in low and high humidities at room temperature. Dropcoated films of polycrystalline ZnO (prepared by a solid-state metathesis) show better sensitivity as resistive gas sensors than films obtained by oxidation of electrodeposited Zn. In both cases, they suffer from baseline drift issues and slow recovery times. In contrast, capacitive gas sensing for dropcoated ZnO films shows faster and more repeatable responses than resistive sensing. Our results demonstrate that an increase in ambient humidity increases the

sensitivity and recovery time for the dropcoated films. In order for our materials sensors to be useful in harsh humidity environments, sensors incorporating them would need to be calibrated to account for capacitance baseline differences with relative humidity changes.

## 5.1 Resistive *vs.* capacitive sensing

Resistive sensing is the most commonly used mode for gas detection by ZnO [4]. It is based on monitoring changes in resistance (or current) with time under the application of a fixed bias voltage. Gas sensitivity is due to the interaction between the surface of the sensor and the target gas. Therefore, surface chemistry plays an important role in the gas detection. The ZnO surface, when exposed to air, has a tendency to adsorb oxygen and form  $O_2^-$  [58, 130, 131] by capturing the free electrons from the surface of ZnO. Therefore, ZnO displays high resistances in the presence of these adsorbed oxygen species. Ethanol detection by polycrystalline ZnO is attributed to the reaction between adsorbed  $O_2^-$  and ethanol vapor. Since ethanol is a reducing gas, it reacts with the surface oxygen species and subsequently releases trapped electrons back into the conduction band, which increases the conduction of the sensor [58, 130, 131]. The ZnO samples tested by us also show a decrease in resistance (or increase in current) at fixed bias voltage when exposed to ethanol vapor. Gas sensing studies are typically done at elevated temperature (150–400°C)

due to the low sensitivity at room temperature [132]. At elevated temperatures (above 150°C) the adsorbed oxygen species change from  $O_2^-$  (molecular form) to  $O^-$  and  $O^{2-}$  (atomic forms), which increases sensitivity due to a change in the reaction mechanism [50].

As discussed in Section 2.2.1, ethanol adsorption causes an increase in interfacial capacitance due to an increase in electron concentration.

$$C_{interface} = \sqrt{\frac{q\epsilon n_d}{2\phi_b}} \quad (5.1)$$

Therefore it also shows up in the measured value of capacitance.

$$C_{measured} = A\left(\frac{\epsilon}{thickness} + \Sigma C_{interface}\right) \quad (5.2)$$

Hence, in the case of capacitive gas sensing, changes in the interfacial capacitance ( $C_{interface}$ ) due to adsorption of gas molecules are measured. Due to the very large dielectric constant for water (78.5) [11], the adsorption of water molecules at the grain interfaces will also increase the interfacial capacitance. As a result, the overall capacitance of ZnO increases with an increase in ambient humidity.

## 5.2 Challenges with resistive sensing

Dropcoated ZnO films prepared by solid state metathesis have large forward currents and small reverse currents at moderate humidities ( $40 \pm 7\%$  RH) as shown in Figure 5.1a. This causes orders of magnitude of difference in the baseline resistances

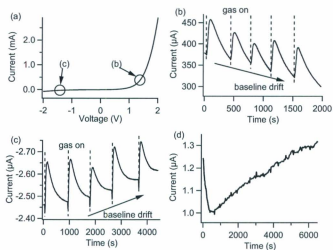


Figure 5.1: (a) Representative current-voltage curve for dropcoated film at  $40\pm 7\%$  RH showing the applied bias voltage (solid circles) at which the sensing data in (b) and (c) is taken. These films show current increases in the presence of ethanol (5000 ppm) at room temperature under (b) forward bias (at  $+1.5$  V) or (c) reverse bias (at  $-1.5$  V). (d) shows an example of baseline drift encountered in resistive sensing (at  $+400$  mV). The baseline drift is evident in all cases, but the direction and magnitude of the drift are not consistent over time. The dashed vertical lines indicate when the target gas was introduced to the measurement chamber.

depending on the applied bias. For example, reverse (negative) bias of  $-1.5$  V gives  $M\Omega$  resistances while forward (positive) bias of  $+1.5$  V give  $k\Omega$ -range baselines. Figure 5.1b,c compares the sensitivity of ZnO to 5000 ppm ethanol at high DC bias (both forward and reverse). It is worth noting that these resistive sensing measurements were taken only after exposing the films to the desired bias for at least 3 hours at  $40\pm 7\%$  RH and room temperature. However, the data shown in the Figure 5.1 and subsequent figures is offset along time axis. This is done to only show the data related to the introduction of ethanol pulses to ZnO films placed inside the measurement chamber. Sensitivities are better for forward bias ( $20\pm 3\%$  at  $+1.5$  V) than for reverse bias ( $8\pm 3\%$  at  $-1.5$  V). These sensitivity values are an order of magnitude lower than that reported for ethanol sensing by ZnO at temperatures of  $\geq 250^\circ\text{C}$  [67]. There is also considerable baseline drift.

There are studies that show baseline drifts associated with resistive gas sensing by ZnO [69,71], and other metal oxide sensors [7]. This drift is due to oxygen adsorption and desorption induced changes in the surface resistance, as explained in Section 2.2.2 [69]. A representative plot of baseline drift encountered in resistive sensing measurements for dropcoated ZnO films tested in humidity controlled chamber with  $40\pm 7\%$  RH at room temperature (without exposing it to ethanol), is shown in Figure 5.1d.

We calculated the sensor recovery times by fitting the current-time data to an exponential function as outlined in Chapter 3. For dropcoated ZnO, recovery time

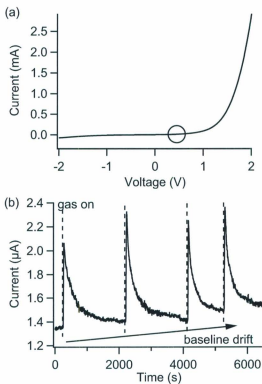


Figure 5.2: DC bias lowering to 400 mV (indicated by the circle in (a)), reduces the baseline drift (shown in (b)) while sensing 10000 ppm ethanol at  $40 \pm 7\%$  RH for the dropcoated film, but does not completely eliminate it. The dashed vertical lines indicate when the target gas was introduced to the measurement chamber.

constant values for ethanol sensing (5000 ppm) at high forward bias voltage are  $300 \pm 20$  seconds, while values drop to  $220 \pm 30$  seconds for high reverse bias voltages. These recovery times are an order of magnitude longer than the ZnO sensors operated at temperature of  $300^\circ\text{C}$  [14,58,133]. This is likely due to the fact that different kinds of adsorbed oxygen species at different temperatures will induce reaction mechanism changes [50]. Typical recovery times for gas sensors available in the market are on the order of 10–20 seconds. It is worth mentioning that the baseline drift is reduced while testing the dropcoated ZnO films at low DC bias (400 mV) for ethanol sensing, but it is not completely eliminated (Figure 5.2b). The baseline drift at low bias was observed every time this measurement was performed even after allowing the sensor to stabilize for upto 8 hours in  $40 \pm 7\%$  RH at room temperature.

Compared with dropcoated films, ZnO films obtained by oxidation show very low resistances (around 50–100  $\Omega$ ), which would be considered ideal for low-power resistive sensing devices. But similar to dropcoated ZnO, these films also suffer from the problems of incomplete recovery to baseline after responding to 5000 ppm ethanol (Figure 5.3). As summarized in Table 5.1, the sensitivity values for these samples at room temperature are much lower than dropcoated films ( $1.4 \pm 0.2\%$ ), but the recovery time constants are not much different.

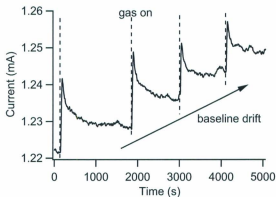


Figure 5.3: Selected responses of ZnO films obtained by oxidation of Zn-metal to 5000 ppm ethanol at  $40\pm 7\%$  RH show an incomplete recovery to baseline even at 100 mV bias voltage. The dashed vertical lines indicate when the target gas was introduced to the measurement chamber.

Table 5.1: Comparison of resistive ethanol (5000 ppm) sensitivity and recovery times for ZnO films at  $40\pm 7\%$  RH.

Synthesis	Sensitivity (%)	Recovery time (s)
Solid state metathesis at positive bias	$20\pm 3$	$300\pm 20$
Solid state metathesis at negative bias	$8\pm 3$	$220\pm 30$
Zn metal oxidation	$1.4\pm 0.2$	$200\pm 40$

### 5.3 Successes with capacitive sensing

The problems of significant baseline drift disappear and recovery times are much faster when our ZnO films are used as capacitive sensors. Furthermore, while exploring this mode of sensing in detail, we also find interesting trends pertaining to moisture effect on sensing responses. It is worth noting that, due to our instrument's limitations with large capacitance values, the 10-100  $\mu\text{F}$  values for ZnO films obtained by oxidation were too large for us to measure.

Careful experiments show that ambient humidity plays an important role in sensitivity and recovery times of our ZnO films. We find that there is a humidity range (near  $40 \pm 7\%$  RH) where the sensitivity and recovery time constant for the 5000 ppm ethanol are optimum (Figure 5.4). Below this humidity range, the signal-to-noise ratio is too low and hence sensitivity is very low. Above this humidity range the sensitivity is high but the recovery time constant is longer (Table 5.2). However, these recovery times are still faster than those reported for room temperature sensing of ethanol by polycrystalline ZnO prepared by other methods [57]. In comparison to resistive sensing, the capacitive sensing for the same dropcoated films show an order of magnitude lower recovery time constant.

As discussed earlier, the capacitance changes for ZnO films are due to changes in dielectric constant after exposure to ethanol. However, ambient humidity changes also affect the dielectric constant because of water's large dielectric constant (78.5

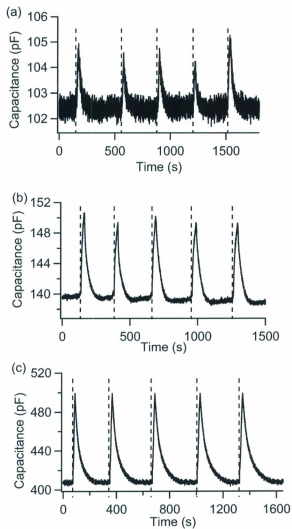


Figure 5.4: Selected responses of dropcoated ZnO films to 5000 ppm ethanol at (a) 15% RH (b) 40% RH (c) 65% RH. The uncertainty in RH is  $\pm 7\%$ . Dashed lines indicate when a 10 s ethanol pulse was introduced to the sensor.

Table 5.2: Variation of capacitive ethanol sensitivity (at 5000 ppm) and recovery times at different humidities for dropcoated ZnO films.

Humidity (%RH)	Sensitivity (%)	Recovery time constant (s)
15±7	2±0.5	20±5
40±7	7±1	30±10
60±7	20±2	60±15

at room temperature [11]). For this reason, the capacitance baseline increases with increasing relative humidity. Therefore, analysis of sensitivity and recovery time constant as a function of ambient humidity is important. It highlights the fact that capacitive sensors based on ZnO might be most useful if kept at a single relative humidity in order to get reliable and reproducible responses to a target gas. Strategies for achieving this goal are discussed in Chapter 7.

In summary, capacitive sensing by our dropcoated ZnO films offer advantages of eliminating baseline drift as well as faster responses compared to resistive sensing.

## Chapter 6

# Ambient Humidity Effects on ZnO Electrical Properties

Results in Chapter 5 show that our ZnO samples, when synthesized by a solid-state metathesis reaction, have better potential as a capacitive rather than resistive sensing material. This chapter explores the physics behind these performance differences. Ambient humidity plays a key role in the sensing response, which has implications for applied uses of ZnO even beyond sensing devices. We show that ZnO obtained by oxidation of Zn metal shows negligible humidity impact on its electrical responses. In contrast, solid-state synthesized ZnO shows significant changes in electrical responses under different humidity conditions that can be linked with water electrolysis.

## 6.1 Synthesis tuning to mitigate humidity effects

ZnO is known to be slightly soluble in water [29,30]. Therefore, it is not surprising to see that changes in ambient humidity can affect the conductivity of ZnO [31,109,110,134]. In Chapter 4, I described the synthesis details of ZnO films obtained by oxidation of Zn metal. These ZnO films show only slight changes in current–voltage ( $I$ – $V$ ) responses with increasing humidity (Figure 6.1). This is a surprising result compared with the changes we see in solid–state synthesized ZnO (which is described in next section).

The differences in the humidity reactivity of ZnO synthesized by different methods are likely influenced by different crystallite morphologies (Figure 6.2). Needle-like structures in ZnO tend to maximize non-polar surfaces such as  $(10\bar{1}0)$  and  $(11\bar{2}0)$  [65]. It has been reported that these low energy, non-polar surfaces have less surface reactivity to water than polar surfaces [27,47], which leads to different sensitivity to ambient humidity. Therefore, the prevalence of needle morphologies in ZnO obtained by Zn metal oxidation may be a reason why this preparation yields material that is less prone to ambient humidity changes.

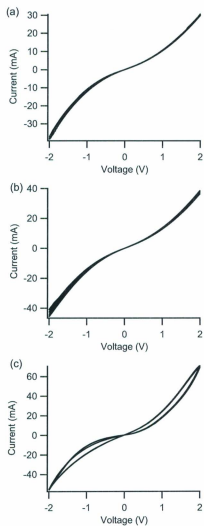


Figure 6.1: Current-voltage responses for ZnO obtained by oxidation of Zn metal at relative humidities of (a)  $15\pm 7\%$  RH, (b)  $40\pm 7\%$  RH and (c)  $65\pm 7\%$  RH. Each plot shows 5 sweeps.

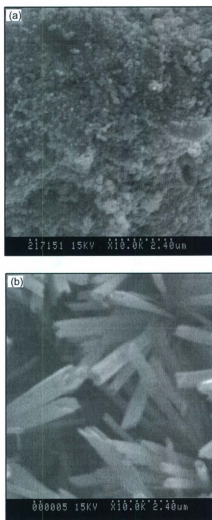


Figure 6.2: SEM images of (a) ZnO obtained by a solid-state metathesis reaction, and (b) ZnO obtained by oxidation of Zn metal. Needle-like morphologies are prevalent in (b).

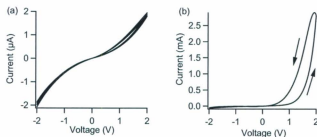


Figure 6.3: Hysteretic current *vs.* voltage responses for a drop-coated ZnO film on steel substrate at (a) 15% RH and (b) 40% RH, are likely due to the presence of adsorbed water. The arrows in (b) indicate the direction of increasing and decreasing current with the voltage.

## 6.2 Impact of humidity on solid state synthesized ZnO

### 6.2.1 DC current-voltage responses

The current-voltage ( $I$ - $V$ ) responses for dropcoated films of solid state synthesized ZnO are drastically different when tested under dry (15% RH) and moderate (40% RH) ambient humidity conditions. Desiccated films show symmetric current-voltage behavior, along with lower current values (Figure 6.3a) and re-hydrating to ambient humidities introduces asymmetry (Figure 6.3b). This trend can be observed by repeating this measurement over several hundred desiccation cycles. In addition to humidity-related changes in DC  $I$ - $V$  responses, we also see the evidence of  $I$ - $V$

Table 6.1: Representative comparison of increase in current with relative humidity based on  $I$ - $V$  data for ZnO films prepared by solid state metathesis and Zn metal oxidation.

Relative humidity	Relative increase in $I$ at 2 V with respect to 15% RH for solid state metathesis	Relative increase in $I$ at 2 V with respect to 15% RH for Zn metal oxidation
40±7% RH	100-1000	2-3
60±7% RH	1000-1500	3-4

hysteresis even in dry (15% RH) conditions (Figure 6.3). This  $I$ - $V$  hysteresis is likely due to water-related electrochemistry [109]. Moreover, as shown in Table 6.1, it is clear that ZnO films prepared by solid state synthesis show 100-1500 times increase in current at moderate (40%) and high humidities (60%). Unlike this, ZnO films obtained by Zn metal oxidation show only 2-4 times increase in current with respect to their current values in dry (15% RH) humidity conditions.

### 6.2.2 Impedance spectroscopy

As mentioned in Chapter 3, AC impedance spectroscopy can be helpful for separating bulk responses (grain interior) from surface responses (grain boundaries and contacts) in polycrystalline materials [113, 114].

The impedance measurements of dropcoated ZnO films show evidence of water-mediated conduction. Figure 6.4a is a representative Nyquist plot for a desiccated sample (at 15±7% RH) that displays a single semicircular arc. We attribute this

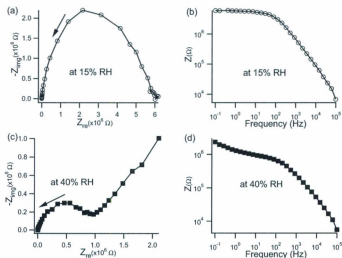


Figure 6.4: Representative (a),(c) Nyquist and (b),(d) Bode plots at  $15 \pm 7\%$  RH (open circles) and  $40 \pm 7\%$  RH (solid squares) for dropcoated ZnO film. The arrows in (a) and (c) indicates the direction of increasing frequency.

feature to grain-boundary controlled conduction, which is often modeled as an equivalent circuit of a resistor and capacitor in parallel [113, 117]. The resistance in such a circuit is related to grain boundary resistance encountered by electrons, whereas the capacitance is linked to the existence of depletion region at the grain boundary [34, 113, 118, 119, 135]. At  $40 \pm 7\%$  RH, the dropcoated films show a semicircle at high frequencies and straight line feature at low frequencies ( $\leq 10$  Hz), as shown in Figure 6.4c. In the case of the straight line feature, impedance increases linearly

with the decrease in applied frequency, known as the Warburg impedance [136].

$$Z_W \propto \frac{1}{\sqrt{\omega}} \quad (6.1)$$

This feature is not typical in solid state impedance measurements, but it is commonly observed in electrochemical impedance data that are obtained in the presence of water or other liquid electrolytes where ions can diffuse easily [137]. Thus, there is a strong indication that the absorbed water is present in reasonable quantity in samples exposed to ambient humidity. Therefore, impedance is controlled by grain boundaries at high frequencies, whereas at low frequencies it is controlled by diffusion of ions present near the grain boundaries.

### 6.3 Interpreting asymmetric $I-V$ responses

Asymmetry observed in  $I-V$  data at moderate humidities ( $\geq 40\%$  RH) for drop-coated ZnO films could be caused by either rectification (Schottky junction between metal contact and ZnO) or by water electrolysis. We now discuss each of these possible explanations. However, before proceeding further with the interpretation of  $I-V$  asymmetry, it is worth mentioning that this asymmetry is not related to electrode area differences, since this effect persists even when the relative areas of the top and bottom electrodes were varied from 1:1.5 to 1:10.

### 6.3.1 Rectification

The  $I$ - $V$  responses in Figure 6.3b look similar to Schottky-like rectification behavior. In order to test the validity of the Schottky-like rectification argument, ZnO was dropcoated on different conducting substrates with a wide range of work functions [100], including Zn (4.4 eV) and Co (5.1 eV). The  $I$ - $V$  responses for these films at 40% RH look qualitatively similar (as shown in Figure 6.5) to those obtained for films on steel substrates.

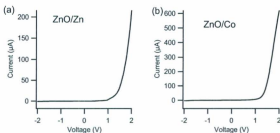


Figure 6.5: ZnO film dropcoated on (a) Zn ( $\phi = 4.4$  eV), and (b) Co ( $\phi = 5.1$  eV) substrates tested at 40% RH show similar responses regardless of substrate work functions.

To quantify differences, these  $I$ - $V$  responses for dropcoated ZnO films on different substrates can be fit to an idealized Schottky relation.

$$I = I_s \exp\left(\frac{e(V - IR)}{nkT}\right) \quad (6.2)$$

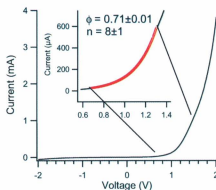


Figure 6.6: Example of an ideal Schottky equation fit of a current–voltage response for dropcoated ZnO at  $40 \pm 7\%$  RH.

By fitting the current voltage data to this equation, barrier height ( $\phi_B$ ) and ideality value ( $n$ ) are extracted. An example of such a fit is shown in Figure 6.6, and the extracted values are summarized in Table 6.2 and shown graphically in Figure 6.7a. The expected values of  $\phi_B$  are calculated by subtracting the ZnO electron affinity value of 3.7 eV [138] from the metal work function values. Comparing the expected  $\phi_B$  values with those extracted from our  $I$ – $V$  data, it is obvious that these values do not agree well. We would have expected barrier voltages to increase as the work function of the substrate increased. Since it did not, it suggests that the  $I$ – $V$  asymmetry is not due to ZnO/substrate Schottky junctions.

Another observation against a Schottky barrier based asymmetry is that  $I$ – $V$  data taken at different relative humidities show a decrease in Schottky barrier height

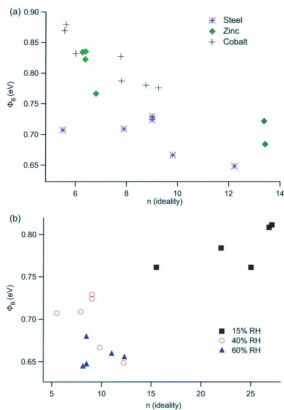


Figure 6.7: Fit parameters of ZnO Schottky barrier heights ( $\phi_B$ ) and ideality factor ( $n$ ), (a) for different substrates (all at 40% RH) and (b) for changes in relative humidities (all on steel substrates).

Table 6.2: Data obtained from fitting  $I$ - $V$  responses at  $40 \pm 7\%$  RH to the ideal Schottky equation. The predicted values of  $\phi_B$  assume a ZnO electron affinity of 3.7 eV and  $n > 1$ .

Substrate	$\phi$ (eV)	$\phi_B$ (eV)	expected $\phi_B$ (eV)
Steel	5.0 [99]	$0.69 \pm 0.03$	1.3
Zinc	4.4 [100]	$0.77 \pm 0.06$	0.7
Cobalt	5.1 [100]	$0.82 \pm 0.04$	1.4

Table 6.3: Data obtained from fitting  $I$ - $V$  responses of dropcoated films on steel substrate at different relative humidities to Schottky equation.

Relative humidity	$\phi_B$	$n$
$15 \pm 7$ %RH	$0.79 \pm 0.02$	$23 \pm 6$
$40 \pm 7$ %RH	$0.70 \pm 0.03$	$9 \pm 4$
$60 \pm 7$ %RH	$0.66 \pm 0.01$	$10 \pm 2$

with the increase in relative humidity as summarized in Table 6.3 and shown graphically in Figure 6.7b. This is not expected because the ZnO/substrate Schottky barrier should not change with variation in atmospheric humidity. Furthermore, the values of  $n$  in Table 6.3 are much larger than unity, which indicates that the non-linearity in our  $I$ - $V$  responses is not close to the ideal Schottky exponential function (for which  $n$  should be equal to 1) [53].

We also note that this current-voltage asymmetry is not observed for all metal oxides. For example, CuO powder (technical grade, BDH) dispersed in ethanol and then dried and tested under similar conditions, did not display asymmetric  $I$ - $V$

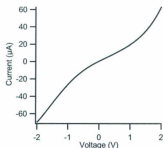


Figure 6.8: Current *vs.* voltage responses for a drop-coated CuO film on a steel substrate in ambient 40% RH.

behavior (Figure 6.8).

### 6.3.2 Electrolysis

The  $I$ - $V$  hysteresis (Figure 6.3) and impedance spectroscopy data (Figure 6.4) suggest that water electrolysis is another possibility for the  $I$ - $V$  asymmetry. During an  $I$ - $V$  measurement, when the ZnO film/substrate interface is positively charged and a ZnO/water vapor interface is negatively charged, water electrolysis would produce  $H_2$  at the ZnO/water vapor interface. Hence, it could be reasonable to fit these  $I$ - $V$  responses with the Butler-Volmer relation (given by Equation 6.3).

$$I = I_0 \exp\left(\frac{n_e(1 - \alpha)F\Delta V}{RT}\right) \quad (6.3)$$

We note that this expression has the same functional form as the Schottky formula given in Equation 6.2. We fit the  $I$ - $V$  curves to Equation 6.3 and extracted a

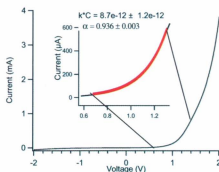


Figure 6.9: Example of current–voltage response (for dropcoated film of ZnO prepared by solid–state synthesis) at  $40 \pm 7\%$  RH, fit to Butler–Volmer equation.

product of heterogeneous rate constant and concentration from the pre-exponential term and the transfer coefficient  $\alpha$  from the exponential term. An example of such a fit, and resulting values obtained from it, are shown in Figure 6.9. A graphical summary is shown in Figure 6.10.

We note that the literature values of  $k^0C_O^{(1-\alpha)}C_R^\alpha$  and  $\alpha$  are reported for the hydrogen evolution reaction in liquid, where voltage is measured against a reference electrode [88]. However, all of our  $I$ – $V$  measurements are done in air without using any reference electrode. Therefore, as a self check, we carried out the hydrogen evolution reaction on dropcoated ZnO film on a steel substrate in 0.1 M KCl without using a reference electrode. Using Equation 6.3 to extract the fit parameters, we find the value for  $k^0C_O^{(1-\alpha)}C_R^\alpha$  for this reaction to be within an order of magnitude from the value obtained for our ZnO in air. Hence, the values of the fit parameters

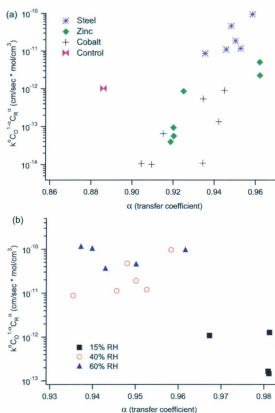


Figure 6.10: Variation in fit parameters  $k^0 C_O^{1-\alpha} C_R^\alpha$  and  $\alpha$  (a) for dropcoated films on steel, zinc and cobalt substrates (all at 40% RH) respectively, and (b) for changes in relative humidity (all on steel substrate). The control in (a) represents the values of fit parameters for ZnO film on steel substrate in 0.1 M KCl solution without a reference electrode.

obtained from Equation 6.3 on  $I$ - $V$  curves for different substrates seem plausible, though we reiterate that these specific values are not meaningful without a true reference electrode.

### 6.3.3 Conclusion

The consistent values obtained for fitted barrier heights ( $\phi_B$ ) on different substrates (at the same relative humidity) suggest that Schottky rectification is not the origin of the observed  $I$ - $V$  asymmetry. In contrast, the trends obtained for product of heterogeneous rate constant and concentration ( $k^0 C_O^{(1-\alpha)} C_R^\alpha$ ) along with the evidence from AC and DC measurements, suggest that water electrolysis is responsible for  $I$ - $V$  asymmetry observed for these dropcoated ZnO films. We infer that there may be preferential absorption of water to the top surface of our ZnO films.

## 6.4 Implications for device applications

The ambient humidity impact on AC and DC electrical responses has implications for ZnO use in device applications, but it does not impede our ability to use polycrystalline ZnO as a capacitive gas sensing element. As mentioned in Chapter 5, the resistive sensing mode suffers from baseline drift as well as slow recovery times. Capacitive sensing at sufficiently high frequencies overcomes these problems because humidity effects (due to water-based ionic conduction) are not important relative to

the intergranular contact impedance at higher operating frequencies such as 3 kHz used in our experiments.

In a broader context, our findings underscore the need for awareness of water interference on electrical responses of metal oxide materials, especially when these are targeted for use in junction based devices [15] and in solar cells [26]. For example, it has been shown that the ambient moisture exposure alters both surface and bulk luminescence of ZnO powders [139]. Therefore, it may be helpful to use such metal oxide materials in controlled humidity environments for reliable and repeatable performance in functional devices. Furthermore, much research effort (mainly on the synthesis front) is needed to lessen water interactions with metal oxide materials. This goal might be achieved either by controlling morphology of these materials to produce crystallites with their less water-reactive faces exposed or encapsulation with a hydrophobic layer to limit the amount of water vapor that reaches the sensor surface [9, 10].

## Chapter 7

### Assessing and Controlling

### Humidity Effects in ZnO-based

### Gas Sensors

Decoupling moisture effects from gas sensing responses is important to improve a sensor's selectivity and reliability in different humidity conditions. This chapter describes the collaborative work that is underway to address this challenge.

#### 7.1 Quantifying ethanol detection sensitivities

In Chapter 5, I described that an increase in ambient humidity enhances the capacitive ethanol sensitivity of solid-state synthesized ZnO. To understand the role

of humidity further, I worked with Jiaqi Cheng (a PhD student in the Poduska research group) to quantify the effect of humidity in ethanol gas on capacitive gas sensitivity and recovery times [140]. A manuscript describing the following work was submitted for peer-review to *Sensors and Actuators B: Chemical* on 10th August 2011. What follows is an extended summary of the submitted manuscript.

Through a series of experiments on solid-state synthesized ZnO films maintained at different relative humidities, we find that increasing the humidity of the chamber or the humidity of the ethanol pulse enhances the capacitive sensitivity. The test chamber humidity was controlled and modified by using different saturated salt solutions (potassium acetate, potassium carbonate or potassium nitrate) to achieve relative humidities of 15%, 40% and 90% respectively. These saturated salt solutions give a characteristic relative humidity value at room temperature [141]. The humidity content of the ethanol vapor (5000 ppm) was modified by mixing water vapor from the saturated air above the aforementioned salt solutions. Therefore, we controlled both the chamber humidity and gas pulse humidity independently. Figure 7.1 shows representative responses when the chamber is maintained at 40% RH. It is clear that when the ethanol pulse contains more moisture, the magnitude of the response increases.

A dry air pulse with 15% RH results in a decrease in capacitance, but an ethanol pulse mixed with dry air increases the capacitance. To explain these observations, it is helpful to consider how the capacitance is related to different parameters in

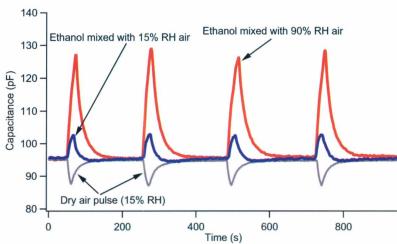


Figure 7.1: Variation in the responses of ZnO at  $40\pm 7\%$  RH with different amounts of moisture mixed in 5000 ppm ethanol. A dry air pulse (with 15% RH) causes a decrease in capacitance.

our sensor. We invoke a parallel plate capacitance model for our ZnO films, where different target species can adsorb.

$$C = A\epsilon_0 \frac{\epsilon_1 + \epsilon_2}{d} \quad (7.1)$$

In Equation 7.1,  $C$  is the effective capacitance,  $\epsilon_0$  is the permittivity of vacuum,  $A$  is the electrode area,  $\epsilon_1$  is the dielectric constant of ZnO,  $\epsilon_2$  is the dielectric constant of the material between the ZnO and the metal electrodes and  $d$  is the separation between metal electrodes [142].  $\epsilon_2$  changes with the variation in humidity and with the type of target gas such as ethanol. In ambient humidity, water vapor adsorbs on ZnO and its dipoles align along the surface, causing an increase in electron concentration [59]. Since water has a high relative dielectric constant ( $\sim 78.5$ ) [11], the capacitance in the presence of moist air will be higher than the measured value in the dry air. The amount of adsorbed water also varies with the relative humidity, and as a result, different baseline capacitances are observed at different humidity levels (Figure 5.4). Likewise, ethanol has a relative dielectric constant of  $\sim 25$  [143] and hence for a given humidity level, capacitance will increase with exposure to ethanol vapor. On the other hand, when the surface is exposed to a dry air pulse, it results in desorption of water vapor from the surface and the capacitance decreases (Figure 7.1).

We can also explain the increase in capacitance of ZnO upon exposure to ethanol vapor based on band structure changes. When as-grown  $n$ -type ZnO is exposed to air, oxygen molecules adsorb on it and form  $O_2^-$  due to electron capture from

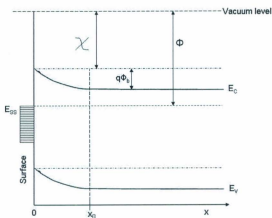


Figure 7.2: Schematic depiction of an energy level diagram of a rectifying oxygen-semiconductor (Schottky) junction. Here  $x$  denotes the distance from the surface, and  $x_0$  indicates the width of the space charge region in ZnO.  $E_C$ ,  $E_F$ , and  $E_V$  indicate the conduction band, Fermi energy, and valence band, respectively.  $E_{SS}$  denote the surface states, that are occupied by adsorbed oxygen species.  $q\phi_b$  denotes the energy barrier encountered by electrons to move from ZnO to the surface oxygen species.  $\phi$  denotes the work function, and  $\chi$  is the electron affinity.

the conduction band [6,58]. This decreases the electron concentration in conduction band and causes band bending along with the creation of an electron depletion region (space charge region), as shown in Figure 7.2 [6, 51]. According to the Schottky barrier model, this depletion region has a capacitance associated with it [53,55,56]. This capacitance is related to electron concentration ( $n$ ) in the bulk and barrier height ( $\phi_b$ ) by following Equation 7.2 [55-57].

$$C \propto \sqrt{\frac{n}{\phi_b}} \quad (7.2)$$

As a result of these adsorbed oxygen species, the capacitance of ZnO is reduced. On the other hand, when the ZnO surface is exposed to ethanol, it interacts with the adsorbed oxygen and the electrons are released back to the conduction band. This increases the electron concentration and decreases the barrier height, thereby increasing the capacitance.

Table 7.1 summarizes the sensitivity values (at 40% RH in the chamber) obtained for ethanol pulses with different relative humidities. These sensitivity values are better than those reported for other ethanol sensors tested at room temperature [144]. Higher sensitivities to ethanol have been achieved by operating the sensor at elevated temperatures (above 150°C) [132]. This is due to the sensing mechanism changing as consequence of adsorbed oxygen species change from  $O_2^-$  (molecular form) to  $O^-$  and  $O^{2-}$  (atomic forms), which increases the sensitivity [50].

It is important to mention that increasing the content of water vapor in the ethanol pulse does not impact the recovery time (Table 7.2). This similarity in

Table 7.1: Variation of capacitive ethanol sensitivity (at 5000 ppm) at 40% RH for ZnO films.

Humidity content in ethanol (%RH)	Sensitivity (%)
15	7±1
40	16±1
90	32±2

Table 7.2: Recovery time data for capacitive ethanol responses (at 5000 ppm) recorded at 40% RH. The water vapor (100% RH) entries correspond to water vapor injection in the chamber at 40% RH and 90% RH, respectively.

Target gas with %RH	Recovery time constant (s)
Ethanol mixed with 15% RH air	18±2
Ethanol mixed with 40% RH air	19±1
Ethanol mixed with 90% RH air	19±2
Water vapor at 40% RH	34±3
Water vapor at 90% RH	77±3

recovery times could be due to the formation of an ethanol-water complex and its subsequent adsorption on the ZnO surface. Earlier studies have shown that ethanol can acquire complex hydration structures due to interaction of water and ethanol in both gas as well as condensed phases [145]. However, the recovery times for water vapor pulses alone are slower in different humidity environments. This increase in recovery time might be because water vapor desorption from the ZnO surface slows down with higher water vapor pressure.

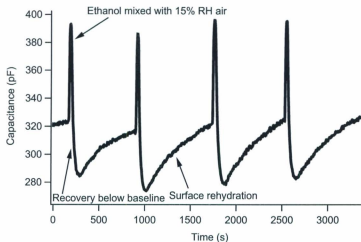


Figure 7.3: Representative responses of ZnO to an ethanol mixture diluted with dry air (15% RH) shows the dehydration of the films in the gradual fall below baseline and subsequent recovery to baseline.

Another interesting effect observed during capacitive ethanol sensing at very high relative humidities (90% RH) is the appearance of a different feature (recovery below baseline) in the recovery stage, as shown in Figure 7.3. This type of recovery feature is not observed in data collected at lower chamber humidities. This feature appears to be related to the large difference in the humidity content of the target gas and the chamber. However, the sensor recovers to the baseline by rehydrating to ambient humidity level. Table 7.3 shows that the sensitivities at 90% RH are even larger than those recorded at 40% RH.

The enhancement of capacitive ethanol sensing responses both with the humidity

Table 7.3: Variation of capacitive ethanol sensitivity (at 5000 ppm) at 90% RH for ZnO films.

Humidity content in ethanol gas pulse (%RH)	Sensitivity (%)
15	20±1
40	31±1
90	50±2

in the target gas as well as ambient chamber humidity has important implications. At very high ambient humidities (90% RH), the largest sensitivities are achieved. However, the sensor is not ready for another sensing event for longer time due to rehydration of ZnO surface to match the ambient humidity. As discussed in Chapter 5, at very low humidities (15% RH) the ethanol sensitivity is very low ( $\sim 2\%$ ). Therefore, the best operating condition for these ZnO sensors is near 40% RH. The trend in sensitivity enhancement with humidity may not be unique to ethanol and may hold true for other reducing gases as well. For example, studies by others on carbon monoxide (CO) show that sensitivity increases with increase in humidity [7]. Other studies show that sensitivity to alcohol increases up to 50% RH, but after that it decreases [73]. It is important to mention that these and other studies have focussed on sensitivity and not recovery properties.

Our studies demonstrate that increasing the moisture content of ethanol gas does not change sensor's recovery times. These findings point to the fact that water vapor not only interacts with the sensing material, but also with the target gas. Since

water is present in many sensing environments, understanding the role of water in gas sensing is essential to improve sensor performance.

## 7.2 Reducing the impact of humidity and improving selectivity with zeolite-coatings

The filtering action of zeolites has been used to improve selectivity of the gas sensors because target gases with different sizes and/or masses will not diffuse at the same rate through them [146]. Furthermore, catalytic conversion of target gases can result in products to which the sensing materials show either enhanced or suppressed responses [10, 147]. In the context of this thesis work, we discuss the role of zeolite coatings as filters on ZnO based sensor element materials.

Zeolites are both naturally occurring as well as synthetically produced materials which consist of porous interconnected aluminosilicate structures [148]. The aluminum and silicon atoms in the zeolites are tetrahedrally coordinated by oxygen [149]. This gives them a net negative charge, which is counteracted by cations such as  $\text{Na}^+$ ,  $\text{Mg}^{2+}$  and  $\text{Ca}^{2+}$  incorporated in the pores [146, 149]. Depending on the size and shape of their pore structure, when they are exposed to different molecules (whether in an electrolyte or air), zeolites may be selective in which molecules can pass through their pores [148]. Different zeolites have varying degrees of water sorption capacity, therefore some zeolites have the potential to filter the humidity from

target stream [149]. Hydrophobicity in zeolites is controlled by the silica to alumina ratio in their structure, and zeolites with larger ratios of silica to alumina tend to be more hydrophobic [149].

Most of the zeolites developed and exploited earlier were for petroleum purification applications [150]. These have small pore sizes ( $\sim 1$  nm) that can be used for catalysis of smaller molecules (such as volatile organic compounds,  $H_2$  and  $O_2$ ) [150]. Following this lead, such catalytically active zeolites have mostly been investigated as coatings on gas sensing materials for these smaller molecules [146, 151–153]. For example, studies by Fukui and Nishida on  $La_2O_3$ -Au:SnO<sub>2</sub> coated with a zeolite known as ferrierite show a selective response towards carbon monoxide over ethanol [151]. This was attributed to the catalytic conversion of ethanol to ethylene, to which the sensing layer shows smaller sensitivity [151]. Mann *et al.* used a coating of zeolite on  $Cr_{2-x}Ti_xO_y$  and achieved improved selectivity for nonane gas compared to other alkanes (such as heptane, octane and decane) [152]. This was attributed to conversion of nonane to methyl propane and water, to which this sensing material displays enhanced sensitivity [152]. Binions *et al.* demonstrated that coating zeolite on the surface of  $Cr_{1.95}Ti_{0.05}O_3$  and  $WO_3$  improves selectivity toward ethanol gas over isopropyl alcohol [10]. This was attributed to a catalytic reaction of ethanol in the zeolite layer [10].

Much of the research work (some of which is described above) on the development and use of zeolite coatings on gas sensing materials has focused on improving

selectivity toward a particular target gas. However, there is a need for identifying and modifying zeolite coatings in a way that they can simultaneously improve selectivity and reduce the interference of ambient humidity on gas sensing responses of oxide materials. To this end, we have started a collaboration with Dr. Bionions (University College London, and Queen Mary University of London) to investigate how ambient humidity effects can be reduced with the use of zeolite coatings on our ZnO samples.

## Chapter 8

# Summary, Conclusions, and Broader Contexts

### 8.1 Summary and conclusions

My thesis work has assessed and addressed the challenges of working with polycrystalline ZnO in variable humidity environments by correlating synthesis, structure, and physical properties. Furthermore, I have also explored how to circumvent the problems associated with the use of this material as a gas sensor in ambient environments. The effects of humidity were investigated by looking at three specific parameters: baseline drift, sensitivity, and response time. For this purpose, the humidity in the measurement chamber as well as in the target gas stream was changed. At moderate chamber humidities ( $\sim 40\%$  RH), resistive sensing on solid state synthe-

sized films gave longer recovery times (on the order of several hundred seconds) and showed resistance baseline drifts. In contrast, the corresponding capacitive sensing measurements gave shorter recovery times (tens of seconds), and showed no baseline drift with comparable sensitivities. Due to the superior performance of our films in capacitive sensing mode, the effects of chamber and gas humidity were explored in more detail in this measurement mode.

For capacitive sensing measurements, increasing the chamber humidity as well as humidity content of the ethanol enhances the sensitivity without changing the recovery times. On the other hand, recovery time to water vapor alone was longer than for ethanol-water vapor mixtures. These findings point to the fact that water vapor possibly interacts with the target gas in addition to the sensing material. Moreover, at very high chamber humidities (90% RH), we observe another phenomena that is surface de-hydration and subsequent re-hydration in the recovery stage of ethanol sensing responses. The appearance of this feature in the recovery stage is clearly linked to the difference in the moisture content of the target gas and the chamber humidity. Based on these findings, we propose the optimum humidity conditions for capacitive sensing for our ZnO films to be around 40% RH. We conclude that our ZnO films work better as capacitive sensors in ambient humidities; however, humidity influences the sensing properties in a non-trivial way. Further work needs to be done to understand the interaction of water vapor with the sensing material as well as the target gas.

In order to find out whether the impact of humidity is inherent to bulk ZnO or if surface factors are also playing a role, we compared the electrical properties of ZnO prepared by solid state metathesis with Zn metal oxidation. It is worth mentioning that both preparation methods yield crystalline ZnO, but solid state metathesis gives crystallites with granular morphologies with ill-defined faces, while Zn metal oxidation gives a needle-like crystallite morphology. Comparing the current-voltage ( $I-V$ ) responses in different humidity conditions for both preparation methods, solid state synthesized ZnO films are influenced more by ambient humidity than the ZnO obtained by oxidation. The current values obtained for solid state synthesized ZnO in moderate (40% RH) and high humidity (60% RH) conditions were three orders of magnitudes higher than the values in dry (15% RH) conditions. On the other hand, films obtained by oxidation only showed less than an order of magnitude increase in current under the aforementioned humidity conditions.

Solid state synthesized ZnO films also display asymmetric  $I-V$  responses under moderate and high humidity conditions. Analysis of  $I-V$  data for these films revealed that the observed asymmetry is due to preferential absorption of water vapor at the top surface of films and its subsequent electrolysis. Based on these comparisons, it is clear that synthesis tuning does have an impact on the electrical properties of these ZnO films under different humidity conditions. However, to ascertain the exact role of crystallite size and morphology on the properties of ZnO under different humidity conditions, further work needs to be done.

## 8.2 Future work and broader contexts

This thesis work highlights the challenges of working with a single material as a gas sensing element in different ambient environments. Most semiconductor metal oxides are known to suffer from poor selectivity among different target gases [4, 6]. Therefore, the true solution to realize a reliable gas sensor likely lies beyond a single gas sensing element and in the use of a sensing array. A sensing array should consist of different sensing elements, such that each member of the array shows a distinguishably different response to a target gas. Some transition metal oxides such as  $\text{MoO}_3$  and  $\text{WO}_3$  are not sensitive to all gases. For instance,  $\text{MoO}_3$  is not sensitive to CO, and  $\text{WO}_3$  is not sensitive to gases like  $\text{SO}_2$  and propanol [4]. These metal oxides in conjunction with ZnO could be used in a sensing array. If this array is exposed to a particular gas, the sensing response by each member of the array will be different for this gas. These responses can then be fed to pattern recognition software for analysis and identification. This concept has been explored before to improve selectivity [1, 154]. However, two major challenges are associated with such an approach. One is the synthesis of different materials for the array and fitting them together on the sensing platform is scientifically challenging. The second challenge is developing pattern recognition software that has the capability of storing and sorting the responses of sensing elements in the array and subsequent analysis.

To obtain a clear understanding on the role of crystallite morphology on the

properties of polycrystalline ZnO, structures with preferentially exposed polar and non-polar surfaces could be synthesized using a technique demonstrated by Joo *et al.* [78]. By using tools like a Kelvin Probe Microscope (KPM), the effect of various ambient and gas humidity environments on the surface states of preferentially exposed polar and non-polar surfaces could be tracked. A Kelvin Probe Microscope is a scanning probe tool similar to the Atomic Force Microscope (AFM). In this method, a metallic tip electrically coupled with the sample surface is scanned over it at a constant distance. The difference between the work functions of the tip and the sample surface results in a potential difference, and hence in an electric force. This force can be eliminated by applying an external bias voltage that has the same magnitude as the contact potential but an opposite polarity. This external bias that eliminates the force due to the contact potential is equal to the difference in work function between the tip and the sample. In this way the work function of the sample surface can be calculated, if the work function of the tip is known [7]. Comparing the KPM data for preferentially exposed polar surface and non-polar surface samples under different ambient and gas humidity conditions could provide information about which crystallite morphology are more prone to these changes. Moreover, it will also give us information about how the ethanol-water vapor mixture is impacting these surfaces.

ZnO has applications in optical (solar cells [26]) and electronic devices (light emitting diodes [15]). For these applications, interactions between ZnO and its ambient

environment can be very undesirable and lead to performance challenges, if they alter the optical and electronic responses. ZnO samples targeted for the aforementioned applications could be systematically studied under different humidity conditions with infrared spectroscopy to assess changes in surface adsorbates. Infrared spectroscopy (IR) is used to study the different vibrational modes in solids [155]. In this approach, ZnO samples should be stored under different humidity conditions. The infrared spectrum of surface of the samples stored under different humidity conditions should be obtained at regular intervals (of few weeks) and comparisons should be made among these spectra. Storage in moderate to high ambient humidities can lead to chemical changes like formation of hydroxyls or carbonates on the surface of ZnO [29]. These adsorbed surface species have typical signatures in the IR spectra [155]. For instance, IR studies by others show that hydroxylation of ZnO surface results in sharp OH stretching vibrations at around  $3600\text{ cm}^{-1}$ , which are typically absent in hydroxyl-free ZnO surface [156]. Therefore, one could track the adsorption of these species under various humidity conditions with time. Such a study could be helpful in determining the humidity range and the time for which these ZnO materials could be used in aforementioned applications without the risk of degradation.

Another useful study would be to follow the effect of particle size and grain boundaries in different ambient humidity environments on the electrical properties using the impedance spectroscopic measurements. Some studies explore the effect

of grain boundaries on the electrical properties using impedance spectroscopy at high temperatures [34,157]. We have found from  $I$ - $V$  data that annealed solid state synthesized ZnO (with larger particles) is little less sensitive to ambient humidity. Annealing at 850°C is the optimum temperature where grain growth occurs with minimum weight loss for ZnO powders [158]. The AC impedance spectroscopy behavior of the annealed samples could be recorded under different humidity conditions as well as in the presence of ethanol vapor. AC impedance studies are helpful in identifying the bulk and surface contributions to the electrical properties, so changes observed in the impedance behavior will help us understand the role of grain boundaries on the adsorption processes in different environments. It is worth mentioning that AC impedance studies are impacted by measurement history, therefore such measurements must be repeated few times and sufficient time should be given between each measurement to obtain consistent results.

## Bibliography

- [1] Srivastava, A. *Sensors and Actuators B: Chemical* **2003**, *96*, 24–37.
- [2] Yamazoe, N. *Sensors and Actuators B* **2005**, *108*, 2–14.
- [3] Gardner, J. W.; Guha, P. K.; Udrea, F.; Covington, J. A. *IEEE Sensors Journal* **2010**, *10*, 1833–1848.
- [4] Eranna, G.; Joshi, B. C.; Runthala, D. P.; Gupta, R. P. *Critical Reviews in Solid State and Materials Sciences* **2004**, *29*, 111–188.
- [5] Korotcenkov, G. *Materials Science and Engineering B* **2007**, *139*, 1–23.
- [6] Barsan, N.; Koziej, D.; Weimer, U. *Sensors and Actuators B* **2007**, *121*, 18–35.
- [7] Barsan, N.; Weimar, U. *Journal of Physics: Condensed Matter* **2003**, *15*, R813–R839.
- [8] Yuan, Q.; Zhao, Y.-P.; Li, L.; Wang, T. *Journal of Physical Chemistry C* **2009**, *113*, 6107–6113.

- [9] Binions, R.; Davies, H.; Afonja, A.; Dungey, S.; Lewis, D.; Williams, D. E.; Parkin, I. P. *Journal of The Electrochemical Society* **2009**, *156*, J46-J51.
- [10] Binions, R.; Afonja, A.; Dungey, S.; Lewis, D. W.; Parkin, I. P.; Williams, D. E. *IEEE Sensors Journal* **2011**, *11*, 1145-1151.
- [11] Ishihara, T.; Matsubara, S. *Journal of Electroceramics* **1998**, *4*, 215-228.
- [12] Cao, Y.; Hu, P.; Pan, W.; Huang, Y.; Jia, D. *Sens. Actuators B* **2008**, *134*, 462-466.
- [13] Ishihara, T.; Sato, S.; Takita, Y. *Sens. Actuators B* **1995**, *24-25*, 392-395.
- [14] Xu, J.; Zhang, Y.; Chenc, Y.; Xiang, Q.; Pan, Q.; Shi, L. *Materials Science and Engineering B* **2008**, *150*, 55-60.
- [15] Özgür, Ü.; Alivov, Y. I.; Liu, C.; Teke, A.; Reshchikov, M. A.; Doğan, Avrutin, V.; Cho, S.-J.; Morkoç, H. *J. Appl. Phys.* **2005**, *98*, 041301.
- [16] Ren, T.; Baker, H. R.; Poduska, K. M. *Thin Solid Films* **2007**, *515*, 7976-7983.
- [17] Dantas, N. O.; dos Santos, M. A. C.; Cunha, F.; Macedo, M. A. *Physica B* **2007**, *398*, 291-293.
- [18] Prasad, V.; D'Souza, C.; Yadav, D.; Shaikh, A. J.; Vigneshwaran, N. *Spectrochimica Acta Part A* **2006**, *65*, 173-178.

- [19] Powder Diffraction File, "Joint Commission on Powder Diffraction Standards – International Centre for Diffraction Data", 2003.
- [20] Ozawa, T. C.; Sung, J. K. *Journal of Applied Crystallography* **2003**, *90*, 679.
- [21] Van de Walle, C. G. *Physical Review Letters* **2000**, *85*, 1012-1015.
- [22] Gupta, T. K. *Journal of American Ceramic Society* **1990**, *73*, 1817-1840.
- [23] Kohan, A. F.; Ceder, G.; Morgan, D.; Van de Walle, C. G. *Physical Review B* **2000**, *61*, 15019-15027.
- [24] Look, D. C.; Hemsley, J. W.; Sizelove, J. R. *Physical Review Letters* **1999**, *82*, 2552-2555.
- [25] Mahalingam, T.; John, V.; Raja, M.; Su, Y.; Sebastian, P. *Solar Energy Materials & Solar Cells* **2005**, *88*, 227-235.
- [26] Ramanathan, K.; Contreras, M. A.; Perkins, C. L.; Asher, S.; Hasoon, F. S.; Keane, J.; Young, D.; Romero, M.; Metzger, W.; Noufi, R.; Ward, J.; Duda, A. *Progress in Photovoltaics: Research and Applications* **2003**, *11*, 225-230.
- [27] Wöll, C. *Progress in Surface Science* **2007**, *82*, 55-120.
- [28] Fabricius, H.; Skettrup, T.; Bisgaard, P. *Applied Optics* **1986**, *25*, 2764-2767.

- [29] Pan, Z.; Tao, J.; Zhu, Y.; Huang, J.-F.; Paranthaman, M. P. *Chemistry of Materials* **2010**, *22*, 149–154.
- [30] Ali, M.; Winterer, M. *Chemistry of Materials* **2010**, *22*, 85–91.
- [31] Traversa, E.; Bearzotti, A. *Sensors and Actuators B* **1995**, *23*, 181–186.
- [32] Liu, Y.; Gorla, C. R.; Liang, S.; Emanetoglu, N.; Lu, Y.; Shen, H.; Wraback, M. *Journal of Electronic Materials* **2000**, *29*, 69–74.
- [33] Heo, Y. W.; Varadarajan, V.; Kaufman, M.; Kim, K.; Norton, D. P.; Ren, F.; Fleming, P. H. *Applied Physics Letters* **2002**, *81*, 3046–3048.
- [34] Kim, S.; Maier, J. *Electrochemical and Solid-State Letters* **2003**, *6*, J7–J9.
- [35] Villanueva, Y. Y.; Liu, D.-R.; Cheng, P. T. *Thin Solid Films* **2006**, *501*, 366–369.
- [36] Lu, J.; Ng, K. M.; Yang, S. *Industrial & Engineering Chemistry Research* **2008**, *47*, 1095–1101.
- [37] Zhu, Y.; Zhou, Y. *Applied Physics A* **2008**, *92*, 275–278.
- [38] Satiennattanakoon, C.; Yiamsawas, D.; Kangwansupamonkon, W.; Nuisin, R. *Advanced Materials Research* **2008**, *55–57*, 657–660.
- [39] Jin, C.-F.; Yuan, X.; Ge, W.-W.; Hong, J.-M.; Xin, X.-Q. *Nanotechnology* **2003**, *14*, 667–669.

- [40] Sun, Z.-P.; Liu, L.; Zhang, L.; Jia, D.-Z. *Nanotechnology* **2006**, *17*, 2266-2270.
- [41] Rout, C. S.; Krishna, S. H.; Vivekchand, S. R. C.; Govindaraj, A.; Rao, C. N. R. *Chemical Physics Letters* **2006**, *418*, 586-590.
- [42] Alivov, Y.; Chernykh, A.; Chukichev, M.; Korotkov, R. *Thin Solid Films* **2005**, *473*, 241-246.
- [43] Panchakarla, L. S.; Shah, M. A.; Govindaraj, A.; Rao, C. N. R. *Journal of Solid State Chemistry* **2007**, *180*, 3106-3110.
- [44] Qiu, Z.; Nadamura, Y.; Ishiguro, T. *Thin Solid Films* **2010**, *518*, 5912-5915.
- [45] Ozawa, K.; Sawada, K.; Shirotori, Y.; Edamoto, K. *Physical Review B* **2003**, *68*, 125417.
- [46] Møller, P. J.; Komolov, S. A.; Lazneva, E. F. *Journal of Physics: Condensed Matter* **1999**, *11*, 9581-9588.
- [47] Al-Sunaidi, A.; Goumri-Said, S. *Chemical Physics Letters* **2011**, *507*, 111-116.
- [48] Look, D. C.; Claffin, B.; Smith, H. E. *Applied Physics Letters* **2008**, *92*, 122108.
- [49] Strzheimchny, Y. M.; Mosbacker, H. L.; Look, D. C.; Reynolds, D. C.; Litton, C. W.; Garces, N. Y.; Giles, N. C.; Halliburton, L. E.; Niki, S.; Brillson, L. J. *Applied Physics Letters* **2004**, *84*, 2545-2547.

- [50] Barsan, N.; Weimar, U. *Journal of Electroceramics* **2001**, *7*, 143–167.
- [51] Wang, C.; Yin, L.; Zhang, L.; Xiang, D.; Gao, R. *Sensors* **2010**, *10*, 2088–2106.
- [52] Neamen, D. A. *An Introduction to Semiconductor Devices*; McGraw-Hall: Boston, 2006.
- [53] Sze, S. M. *Physics of Semiconductor Devices*; John Wiley: New York, 1981.
- [54] Franke, M. E.; Koplín, T. J.; Simon, U. *small* **2006**, *2*, 36–50.
- [55] Lu, F.; Gong, D.; Wang, J.; Wang, Q.; Sun, H.; Wang, X. *Physical Review B* **1996**, *53*, 4623–4629.
- [56] Ponce, M. A.; Castro, M. S.; Aldao, C. *Materials Science and Engineering B* **2004**, *111*, 14–19.
- [57] Zhou, X.; Li, J.; Ma, M.; Xue, Q. *Physica E: Low-dimensional Systems and Nanostructures* **2011**, *43*, 1056 – 1060.
- [58] Wan, Q.; Li, Q. H.; Chen, Y. J.; Wang, T. H.; He, X. L.; Li, J. P.; Lin, C. L. *Applied Physics Letters* **2004**, *84*, 213111.
- [59] Boyle, J. F.; Jones, K. A. *Journal of Electronic Materials* **1977**, *6*, 717–733.
- [60] Bai, H.; Shi, G. *Sensors* **2007**, *7*, 267–307.

- [61] Arshak, K.; Moore, E.; Lyons, G.; Harris, J.; Clifford, S. *Sensor Review* **2004**, *24*, 181–198.
- [62] Seiyama, T.; Kato, A.; Fujiishi, K.; Nagatani, M. *Analytical Chemistry* **1962**, *34*, 1502–1503.
- [63] Eriksson, J.; Khranovskyy, V.; Söderlind, F.; Käll, P.-O.; Yakimova, R.; Spetz, A. L. *Sensors and Actuators B: Chemical* **2009**, *137*, 94–102.
- [64] Ahn, M. W.; Park, K. S.; Heo, J. H.; Park, J. G.; Kim, D. W.; Choi, K. J.; Lee, J. H. *Applied Physics Letters* **2008**, *93*, 263103.
- [65] Wang, Z. L. *Journal of Physics: Condensed Matter* **2004**, *16*, R829–R858.
- [66] Hu, Y.; Zhou, J.; Yeh, P.-H.; Li, Z.; Wei, T.-Y.; Wang, Z. L. *Advanced Materials* **2010**, *22*, 3327–3332.
- [67] Cao, Y.; Pan, W.; Zong, Y.; Jia, D. *Sensors and Actuators B* **2009**, *138*, 480–484.
- [68] Kang, B. S.; Wang, H.; Tien, L.; Ren, F.; Gila, B. P.; Norton, D. P.; Abernathy, C. R.; Lin, J.; Pearton, S. J. *Sensors* **2006**, *6*, 643–666.
- [69] Min, Y. *Properties and sensor performance of ZnO thin films*; Massachusetts Institute of Technology: Cambridge, MA, PhD dissertation ed.; 2003.

- [70] Khranovskyy, V.; Eriksson, J.; Lloyd-Spetz, A.; Yakimova, R.; Hultman, L. *Thin Solid Films* **2009**, *517*, 2073-2078.
- [71] Kobrinsky, V.; Fradkin, E.; Lumelsky, V.; Rothschild, A.; Komem, Y.; Lifshitz, Y. *Sensors and Actuators B: Chemical* **2010**, *148*, 379 - 387.
- [72] Yadav, B. C.; Srivastava, R.; Dwivedi, C. D.; Pramanik, P. *Sensors and Actuators B* **2008**, *131*, 216-222.
- [73] Bai, Z.; Xie, C.; Hub, M.; Zhang, S.; Zeng, D. *Materials Science and Engineering B* **2008**, *149*, 12-17.
- [74] Kobrinsky, V.; Rothschild, A.; Lumelsky, V.; ; Komem, Y.; Lifshitz, Y. *Applied Physics Letters* **2008**, *93*, 113502.
- [75] Marotti, R. E.; Bojorge, C. D.; Broitman, E.; Cánepa, H. R.; Badán, J. A.; Dalchiele, E. A.; Gellman, A. J. *Thin Solid Films* **2008**, *517*, 1077-1080.
- [76] Izaki, M.; Omi, T. *Applied Physics Letters* **1996**, *68*, 2439-2440.
- [77] Shang, T.-M.; Sun, J.-H.; Zhou, Q.-F.; Guan, M.-Y. *Crystal Research and Technology* **2007**, *42*, 1002-1006.
- [78] Joo, J.; Chow, B. Y.; Prakash, M.; Boyden, E. S.; Jacobson, J. M. *Nature Materials* **2011**, *10*, 596-601.
- [79] Wiley, J. B.; Kaner, R. B. *Science* **1992**, *255*, 1093-1097.

- [80] Ye, X. R.; Jia, D. Z.; Yu, J. Q.; Xin, X. Q.; Xue, Z. *Adv. Mater.* **1999**, *11*, 941–942.
- [81] Liu, Y.-L.; Liu, Z.-M.; Yang, Y.; Yang, H.-F.; Shen, G.-L.; Yu, R.-Q. *Sens. Actuators B* **2005**, *107*, 600–604.
- [82] Tan, E.; Ho, G.; Wong, A.; Kawi, S.; Wee, A. *Nanotechnology* **2008**, *19*, 255706/1–7.
- [83] Goto, S.; Fujimura, N.; Nishihara, T.; Ito, T. *Journal of Crystal Growth* **1991**, *115*, 816–820.
- [84] Pan, Z. W.; Dai, Z. R.; Wang, Z. L. *Science* **2001**, *291*, 1947–1949.
- [85] Huang, M. H.; Wu, Y.; Feick, H.; Tran, N.; Weber, E.; Yang, P. *Advanced Materials* **2001**, *13*, 113–116.
- [86] Wang, Z. L. *Materials Today* **2004**, *7*, 26–33.
- [87] Lide, D. R. *CRC Handbook of Chemistry and Physics*; CRC press: Florida, 82nd ed.; 2002.
- [88] Bard, A. J.; Faulkner, L. R. *Electrochemical methods : fundamentals and applications*; John Wiley: New York, 2001.
- [89] Pourbaix, M. *Atlas of Electrochemical Equilibria in Aqueous Solutions*; Pergamon Press: New York, 1966.

- [90] Noel, M.; Vasu, K. I. *Cyclic Voltammetry and the frontiers of electrochemistry*; Aspect Publication Ltd.: London, UK, 1990.
- [91] Kitano, M.; Oktabe, T.; Shiojiri, M. *Journal of Crystal Growth* **1995**, *152*, 73–78.
- [92] Peulon, S.; Lincot, D. *Journal of Electrochemical Society* **1998**, *145*, 864–874.
- [93] Marotti, R. E.; Guerra, D. N.; Bello, C.; Machado, G.; Dalchiele, E. A. *Solar Energy Materials & Solar Cells* **2004**, *82*, 85–103.
- [94] Riveros, G.; Gómez, H.; Henríquez, R.; Sshrebler, R.; Córdova, R.; Marotti, R. E.; Dalchiele, E. *Boletín de la Sociedad Chilena de Química* **2002**, *47*,.
- [95] Ashcroft, N. W.; Mermin, N. D. *Solid State Physics*; Brooks/Cole Thomas Learning: Australia, 1976.
- [96] Kittel, C. *Introduction to Solid State Physics*; John Wiley: New York, USA, 1996.
- [97] Wang, Z. L.; Zhou, W. *Scanning Microscopy for Nanotechnology: Techniques and Applications*; Springer: New York, USA, 1st ed.; 2007.
- [98] Smith, W. F. *Principles of Materials Science and Engineering*; McGraw-Hill: New York, USA, 3rd ed.; 1996.

- [99] Surplice, N. A.; Arcy, R. J. D. *Journal of Physics F: Metal Physics* **1972**, *2*, L8-L10.
- [100] Michaelson, H. B. *J. Appl. Phys.* **1977**, *48*, 4729-4733.
- [101] Kim, S. Y.; Jang, H. W.; Kim, J. K.; Jeon, C. M.; Park, W. I.; Yi, G.-C.; Lee, J.-L. *Journal of Electronic Materials* **2002**, *31*, 868-871.
- [102] Sheng, H.; Emanetoglu, N. W.; Muthukumar, S.; Yakshinskiy, B. V.; Feng, S.; Lu, Y. *Journal of Electronic Materials* **2003**, *32*, 935-938.
- [103] Kim, H.-K.; Kim, K.-K.; Park, S.-J.; Seong, T.-Y. *Journal of Applied Physics* **2003**, *94*, 4225-4227.
- [104] Oh, M. S.; Hwang, D. K.; Lim, J. H.; Choi, Y. S.; Park, S. J. *Applied Physics Letters* **2007**, *91*, 042109.
- [105] Mohanta, K.; Pal, A. J. *Nanotechnology* **2009**, *20*, 185203.
- [106] Gu, Q. L.; Cheung, C. K.; Ling, C. C.; Ng, A. M. C.; Djurichecksić, A. B.; Lu, L. W. *Journal of Applied Physics* **2008**, *103*, 093706.
- [107] von Wenckstern, H.; Rahman, G. B. R. A.; Hochmuth, H.; Lorenz, M.; Grundmann, M. *Applied Physics Letters* **2006**, *88*, 092102.
- [108] Bizzotto, D. "World Wide Web: [www.chem.ubc.ca/personnel/faculty/bizzotto](http://www.chem.ubc.ca/personnel/faculty/bizzotto).", Last accessed October 2009.

- [109] Yoo, D. J.; Park, S. J. *J. Electrochem. Soc.* **1996**, *143*, L89-L91.
- [110] Chatman, S.; Poduska, K. M. *ACS Appl. Mater. Interfaces* **2009**, *1*, 552-558.
- [111] Bockris, J. O.; Reddy, A. K. N.; Gambaio-Aldeco, M. *Modern Electrochemistry: Fundamentals of Electrode Processes*; Kluwer Academic/Plenum Publishers: New York, USA, Second ed.; 2000.
- [112] Zoski, C. G. *Handbook of Electrochemistry*; Elsevier: Oxford, UK, First ed.; 2007.
- [113] Sahay, P. P.; Tewari, S.; Nath, R. K. *Crystal Research and Technology* **2007**, *42*, 723-729.
- [114] You, Y.-H.; So, B.-S.; Hwang, J.-H.; Cho, W.; Lee, S. S.; Chung, T.-M.; Kim, C. G.; An, K.-S. *Applied Physics Letters* **2006**, *89*, 222105.
- [115] Barsoukov, E.; Macdonald, J. R. *Impedance Spectroscopy Theory, Experiment, and Applications*; Wiley-Interscience: USA, 2005.
- [116] Instruments, G. "Basics of Electrochemical Impedance Spectroscopy: <http://www.gamry.com/>", .
- [117] Han, J.; Mantas, P. Q.; Sensos, A. M. R. *Journal of Materials Research* **1995**, *10*, 2295-2300.
- [118] Fleig, J. *Solid State Ionics* **2003**, *161*, 279-289.

- [119] Bueno, P. R.; Varela, J. A.; Longo, E. *Journal of the European Ceramic Society* **2007**, *27*, 4313–4320.
- [120] Carotta, M.; Cervi, A.; di Natale, V.; Gherardi, S.; Giberti, A.; Guidi, V.; Puzzovio, D.; Vendemiati, B.; Martinelli, G.; Sacerdoti, M.; Calestani, D.; Zappettini, A.; Zha, M.; Zanotti, L. *Sensors and Actuators B: Chemical* **2009**, *137*, 164–169.
- [121] Rasheed, M. A.; Poduska, K. M. *Crystal Growth and Design* **2011**, in preparation.
- [122] Chen, S.-W.; Wu, J.-M. *Acta Materialia* **2011**, *59*, 841–847.
- [123] Baruah, S.; Dutta, J. *Journal of Crystal Growth* **2009**, *311*, 2549–2554.
- [124] Sahoo, T.; Tripathy, S. K.; Yu, Y. T.; Ahn, H.-K.; Shin, D.-C.; Lee, I.-H. *Materials Research Bulletin* **2008**, *43*, 2060–2068.
- [125] Chen, J.; Feng, Z.; Ying, P.; Li, M.; Han, B.; Li, C. *Physical Chemistry Chemical Physics* **2004**, *6*, 4473–4479.
- [126] Zhu, P.; Zhang, J.; Wu, Z.; Zhang, Z. *Crystal Growth and Design* **2008**, *8*, 3148–3153.
- [127] Wu, X. L.; Siu, G. G.; Fu, C. L.; Ong, H. C. *Applied Physics Letters* **2001**, *78*, 2285–2287.

- [128] Fang, Z.; Wang, Y.; Xu, D.; Tan, Y.; Liu, X. *Optical Materials* **2004**, *26*, 239-242.
- [129] Studenikin, S. A.; Golego, N.; Cocivera, M. *Journal of Applied Physics* **1998**, *84*, 2287-2294.
- [130] Feng, P.; Wan, Q.; Wang, T. H. *Applied Physics Letters* **2005**, *87*, 213111.
- [131] Jiaqiang, X.; Yuping, C.; Daoyong, C.; Jianian, S. *Sensors and Actuators B: Chemical* **2006**, *113*, 526-531.
- [132] Kanan, S. M.; El-Kadri, O. M.; Abu-Yousef, I. A.; Kanan, M. C. *Sensors* **2009**, *9*, 8158-8196.
- [133] Yang, Z.; Li, L.-M.; Wan, Q.; Liu, Q.-H.; Tai-HongWang, *Sensors and Actuators B: Chemical* **2008**, *135*, 57-60.
- [134] Clafin, B.; Look, D.; Norton, D. R. *Journal of Electronic Materials* **2007**, *36*, 442-445.
- [135] Viswanath, R. N.; Ramasamy, S. N. *Materials Transactions* **2001**, *42*, 1647-1652.
- [136] Plieth, W. *Electrochemistry for Materials Science*; Elsevier: UK, 2008.
- [137] Varghese, O. K.; Grimes, C. A. *J. Nanosci. Nanotech.* **2003**, *3*, 277-293.
- [138] Jacobi, K.; Zwicker, G.; Gutmann, A. *Surface Science* **1984**, *141*, 109-125.

- [139] Liu, M.; Kitai, A. H.; Mascher, P. *Journal of Luminescence* **1992**, *54*, 35–42.
- [140] Cheng, J.; Rasheed, M. A.; Poduska, K. M. *Sensors and Actuators B: Chemical* **2011**, Submitted Aug 2011,.
- [141] Rockland, L. B. *Analytical Chemistry* **1960**, *32*, 1375–1376.
- [142] Grove, T. T.; Masters, M. F.; Miers, R. E. *American Journal of Physics* **2005**, *73*, 52–56.
- [143] Mohsen-Nia, M.; Amiri, H.; Jazi, B. *Journal of Solution Chemistry* **2010**, *39*, 701–708.
- [144] Wu, J. M. *Nanotechnology* **2010**, *21*, 235501.
- [145] Nosko, S. Y.; Lamoureux, G.; Roux, B. *Journal of Physical Chemistry B* **2005**, *109*, 6705–6713.
- [146] Xu, X.; Wang, J.; Long, Y. *Sensors* **2006**, *6*, 1751–1764.
- [147] Vilaseca, M.; Coronas, J.; Cirera, A.; Cornet, A.; Morante, J. R.; Santamaria, J. *Sensors and Actuators B* **2007**, *124*, 99–110.
- [148] Bekkum, H. V.; Flanigen, E. M.; Jansen, J. C. *Introduction to Zeolite Science and Practice*; Elsevier Science Publishers: New York, USA, 1991.
- [149] Chen, N. Y.; Degnan Jr., T. F.; Smith, C. M. *Molecular Transport and*

*Reaction in Zeolites: Design and applications of shape selective catalysts*; John Wiley & Sons Inc.: New York, USA, 1994.

- [150] Xu, R.; Pang, W.; Yu, J.; Huo, Q.; Chen, J. *Chemistry of zeolites and related porous materials: synthesis and structure*; John Wiley & Sons: Singapore, Asia, 2007.
- [151] Fukui, K.; Nishida, S. *Sensors and Actuators B* **1997**, *45*, 101–106.
- [152] Mann, D. P.; Paraskeva, T.; Pratt, K. F. E.; Parkin, I. P.; Williams, D. E. *Measurement Science and Technology* **2005**, *16*, 1193–1200.
- [153] Trimboli, J.; Dutta, P. K. *Sensors and Actuators B* **2004**, *102*, 132–141.
- [154] Wöllenstein, J.; Plaza, J.; Cané, C.; Min, Y.; Böttner, H.; Tuller, H. *Sensors and Actuators B: Chemical* **2003**, *93*, 350–355.
- [155] Keyes, B.; Gedvilas, L.; Li, X.; Coutts, T. *Journal of Crystal Growth* **2005**, *281*, 297–302.
- [156] Noei, H.; Qiu, H.; Wang, Y.; Löffler, E.; Wöll, C.; Muhler, M. *Physical Chemistry Chemical Physics* **2008**, *10*, 7092–7097.
- [157] Nan, C.-W.; Tschöpe, A.; Holten, S.; Kleim, H.; Birringer, R. *Journal of Applied Physics* **1999**, *85*, 7735–7740.

- [158] Mazaheri, M.; Zahedi, A. M.; Sadrnezhad, S. K. *Journal of American Ceramic Society* **2008**, *91*, 56-63.
- [159] O'Hayre, R.; Lee, M.; Prinz, F. B. *Journal of Applied Physics* **2004**, *95*, 8382-8392.
- [160] Glot, A.; Bartolomeo, E. D.; Traversa, E. *Journal of the European Ceramic Society* **1999**, *19*, 715-719.

## Appendix A

### A.1 Bias dependent changes in AC impedance spectra

Dropcoated ZnO films show DC bias dependent changes in addition to humidity-related changes in their impedance spectra. Therefore, we discuss the AC impedance measurement results for two sets of experiments. In one set of experiments involving impedance measurements, the relative humidity was kept at 40% RH (where the  $I$ - $V$  asymmetric response shown in Figure 6.3b are observed) and the DC bias voltage during the measurement was varied from -1 V to 1 V. In another set of experiments, impedance measurements were taken at 15% RH (dry) conditions and the applied DC bias was changed as described above. First, we show that in the relative humidity range of  $40 \pm 7\%$  RH, the AC impedance plots display DC-bias dependent changes (Figure A.1). We note that these measurements have been obtained (and such features observed) on many dropcoated ZnO films and were observed repeatedly

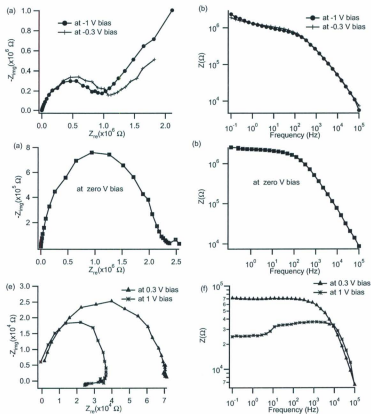


Figure A.1: Bias dependent changes in Nyquist (a,c,e) and Bode plots (b,d,f) at  $40 \pm 7\%$  RH from -1 V to 1 V.

even after measurements at different DC bias voltages.

When the applied DC bias is less than zero, the size of the impedance semicircle in the Nyquist plots decreases (Figure A.1a) but is still larger than the semicircle displayed for positive DC bias values. A negative DC bias gives lower currents (Figure 6.3b), which may correspond to less water electrolysis at the exposed interface. Consequently, as the applied AC frequency is reduced, the capacitive reactance at grain boundary increases and conduction is only due to diffusion of the adsorbed water ions.

For positive DC bias (Figure A.1c) there is no Warburg-like signature. Instead, the size of the impedance semi-circle decreases significantly with increase in bias. O'Hayre *et al.* has observed DC bias dependent reduction in impedance within single grain of a ZnO varistor [159] and Xu *et al.* have observed this decrease in semicircle size with increase in DC bias for a ZnO single crystal nanobelt held between two palladium contacts. They have not mentioned any clear reason for the observed reduction in the size of the impedance semicircle. It is also worth mentioning that the real part of the impedance was reduced by 2 orders of magnitude in comparison to those at negative and zero DC bias. This finding is again consistent with the  $I$ - $V$  responses at 40% RH, where the current is 100-1000 times greater than at negative DC bias. Since positive DC bias means positive voltage at the ZnO/substrate interface and negative polarity at the ZnO/contact and air interface, there is more likelihood of increased electrolysis of adsorbed water molecules and the

corresponding hydrogen evolution reaction at the exposed interface. Consequently, we do not see the Warburg-like signature at the positive DC biases, which means that grain boundary conduction does not go into diffusion control at low frequencies ( $\leq 10$  Hz). At 1 V DC bias, where the turn-on for  $I$ - $V$  responses in dropcoated films occur, in corresponding AC measurements the value of resistance is even lower. There is also evidence of inductive effects at low frequencies.

When the films were desiccated and tested at 15% RH, significant changes in impedance spectra were observed relative to data collected at 40% RH. Figure A.2a shows that there is no Warburg-like signature occurring at negative DC bias at low frequencies and that the size of the impedance semi-circle grows. This is again consistent with  $I$ - $V$  responses where negative bias current decreases by an order of magnitude. Glot *et al.* have observed this type of increase the size of impedance semi-circle with reduction in relative humidity [160], but they have not seen the Warburg-like signature that we observe here. The DC bias dependent changes along with relative humidity induced changes have not been observed synergistically. The reason for the absence of Warburg-like signature at low frequencies at this relative humidity (15% RH) is that at moderate humidity (40% RH) there is enough moisture on the surface and between the grains that limits the low frequency impedance response to diffusion control. Even at this low humidity (15% RH) the size of the impedance semi-circle reduces with increases in DC bias. This is again consistent with the symmetric  $I$ - $V$  behavior observed in this humidity range.

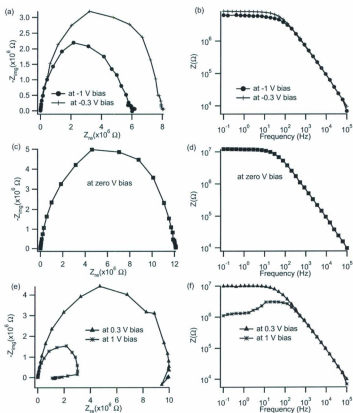


Figure A.2: Bias dependent changes in Nyquist (a,c,e) and Bode plots (b,d,f) at  $15 \pm 7\%$  RH from -1 V to 1 V.

It is evident from above AC impedance observations (at different DC bias and relative humidity conditions) that our solid-state synthesized ZnO films are reacting with absorbed moisture in a non-trivial manner. This underscores the need to control the surface reactivity of ZnO to minimize the interference from ambient moisture for using it as a reliable gas sensing material.





